

# First-principles simulations of the oxidation of methane and CO on platinum oxide surfaces and thin films

von der Fakultät Maschinenwesen

der

Technischen Universität Dresden

zur

Erlangung des akademischen Grades

Doktoringenieur (Dr.-Ing.)

angenommene

## DISSERTATION

vorgelegt von

**Dipl.-Phys. Nicola Seriani**

geboren am 19. März 1977 in Trieste (Italien)

Tag der Einreichung: 31. Januar 2006

Tag der Verteidigung: 20. Juli 2006

Gutachter: Prof. Dr. rer. nat. habil. W. Pompe

Prof. Dr. rer. nat. habil. F. Mertens

Dr.-Ing. L. Colombi Ciacchi

Vorsitzender der

Promotionskommission: Prof. Dr.-Ing. habil. S. Fasoulas



'GALILEI ... Und es ist eine große Lust aufgekommen, die Ursachen aller Dinge zu erforschen: warum der Stein fällt, den man losläßt, und wie er steigt, wenn man ihn hochwirft. Jeden Tag wird etwas gefunden. Selbst die Hundertjährigen lassen sich noch von den Jungen ins Ohr schreien, was Neues entdeckt wurde. Da ist schon viel gefunden, aber da ist mehr, was noch gefunden werden kann. Und so gibt es wieder zu tun für neue Geschlechter.

In Siena, als junger Mensch, sah ich, wie ein paar Bauleute eine tausendjährige Gepflogenheit, Granitblöcke zu bewegen, durch eine neue und zweckmäßigere Anordnung der Seile ersetzten, nach einem Disput von fünf Minuten. Da und dann wusste ich: die alte Zeit ist herum, und es ist eine neue Zeit.'

Bertolt Brecht, *Leben des Galilei*



# Contents

<b>1</b>	<b>Introduction</b>	<b>1</b>
<b>2</b>	<b>Platinum in catalytic converters</b>	<b>5</b>
2.1	Automotive exhaust emission control catalysts . . . . .	5
2.2	Mechanisms of heterogeneous catalytic oxidation . . . . .	7
2.3	Platinum as oxidation catalyst . . . . .	8
<b>3</b>	<b>Computational Methods</b>	<b>13</b>
3.1	Fundamentals of Density Functional Theory . . . . .	14
3.1.1	Adiabatic approximation . . . . .	14
3.1.2	Theorems of Hohenberg and Kohn . . . . .	15
3.1.3	Kohn-Sham equations . . . . .	16
3.2	Ab-initio molecular dynamics . . . . .	18
3.3	Ab-initio thermodynamics . . . . .	18
3.4	Phonons . . . . .	20
3.5	GGA+U . . . . .	22
3.6	Bader charges . . . . .	24
3.7	Calculation details . . . . .	25
<b>4</b>	<b>Structure and thermodynamics of platinum oxides</b>	<b>27</b>
4.1	Bulk platinum oxides . . . . .	27
4.1.1	$\alpha$ -PtO <sub>2</sub> . . . . .	28

4.1.2	$\beta$ -PtO <sub>2</sub> . . . . .	33
4.1.3	Pt <sub>3</sub> O <sub>4</sub> . . . . .	38
4.1.4	PtO . . . . .	39
4.1.5	Ab-initio thermodynamics of bulk oxides . . . . .	42
4.2	Surfaces . . . . .	45
4.3	Thin films . . . . .	47
4.3.1	Pt(111) . . . . .	48
4.3.2	Pt(100) . . . . .	49
4.4	Clusters . . . . .	53
<b>5</b>	<b>Catalysis</b>	<b>57</b>
5.1	Dissociative adsorption of methane . . . . .	57
5.1.1	Dynamics of dissociation . . . . .	61
5.2	CO oxidation . . . . .	64
5.2.1	Energy balance of the Mars-Van Krevelen mechanism . . . . .	69
<b>6</b>	<b>Conclusions</b>	<b>73</b>
6.1	Summary . . . . .	73
6.2	Future works . . . . .	76
	<b>Bibliography</b>	<b>79</b>
	<b>Acknowledgements</b>	<b>87</b>

# Chapter 1

## Introduction

Platinum is a primary element in catalysts for total catalytic oxidation of hydrocarbons and carbon monoxide, which have a large variety of applications like vehicle exhaust emissions control and gas sensors.

There are nonetheless several problems connected with the usage of platinum. First, production is very limited: in the world there are less than ten companies that extract platinum; second, over 90% of world production takes place in only two countries: South Africa and Russia [1]. Demand is increasing steadily and has nearly doubled in the last 15 years. Since consumption in the automotive catalyst industry has increased from 21% of global consumption in 1999 to 44% in 2004, it is evident that it is crucial to develop catalyst technologies able to obtain better rendition of platinum as catalyst and reduce its demand, also in the view that stricter pollution regulations are going to be introduced in the next years, e.g. in Europe.

The big efforts that are under way to understand the atomistic mechanisms of heterogeneous catalytic oxidation on Pt must be put in this context. In the last years several studies have been focused on bridging the pressure-temperature gap between the ultra-high vacuum (UHV) conditions typical for atomistic investigations in surface science and operation conditions of 'real' catalysts. In parallel, developments of simulation techniques and improvements of computer speed have made it possible to study these systems also through

quantum-mechanical simulations. In particular recent computational work has been focused on formation of thin films of transition metal oxides on the surface of catalysts, a phenomenon that is in most cases possible only at high oxygen pressures and therefore represents a feature of catalysts that crucially depends on operation conditions. Formation, structure and catalytic effects of these thin oxide films have been studied in the case of silver [2, 3] and palladium [4], as well as of oxide surfaces [5, 6, 7]. These methods have been proven to have predictive power in the investigation of formation of thin oxide films. A result of paramount importance in these experimental and computational investigations is that oxide formation influences the catalytical activity [3, 8, 9].

In case of platinum, only very recently some papers have appeared that deal with oxide (sub-)monolayer formation on Pt(110) [9] and Pt(111) [10] surfaces on single crystals. Platinum clusters typically have surfaces with (111) and (100) orientations [11].

Despite these efforts, in the currently available literature there is no systematic study that links the formation of a well defined platinum oxide structure to its catalytical activity towards oxidation of hydrocarbons, and it is not clear yet under which conditions platinum oxide phases favour or hinder catalytical activity. This thesis is focused on the formation of oxide on unsupported platinum catalysts under ideal oxygen-rich conditions in absence of poisoning species and its role in oxidation of both methane and CO. To perform this research we have taken advantage of state-of-the-art quantum mechanical simulation techniques, which are a very efficient and reliable computational tool to investigate chemical reactions at the atomic level. While this method cannot give ultimate answers about all aspects of the catalytic process (e.g. sintering in the catalyst), we are confident that the new ideas developed in this thesis will find fruitful technological applications in the next years.

The aims of this thesis are:

- 1) To provide an overall picture of bulk platinum oxides, by systematically studying their structural, electronic and thermodynamic properties.
- 2) To start from this picture to analyze formation, structure and stability of platinum oxide surfaces, both in the case of bulk oxides and of thin oxide films on metal, under oxygen-rich



conditions, as heterogeneous catalysis depends crucially on surface properties.

- 3) To investigate the stability of platinum oxide clusters, focusing in particular on the size-dependence of the transition temperatures between different oxidation states.
- 4) To finalize the previous investigation by determining catalytic behaviour of relevant structures towards oxidation of methane and carbon monoxide.
- 5) To use this information to formulate a proposal to improve existing catalyst technologies.



# Chapter 2

## Platinum in catalytic converters

Typical applications of platinum clusters in heterogenous catalytic oxidation are automotive emission control catalysts and gas sensors. In the latter, oxidation of gases over the clusters leads to production of heat, which is detected and converted to an electric signal, e.g. through pyroelectric switches. The former are described more in detail in the next section.

### 2.1 Automotive exhaust emission control catalysts

A typical exhaust emission control catalyst consists of a ceramic structure (support) through which the exhaust gases can flow [12]. The support is made of a material, typically  $\gamma$ -Al<sub>2</sub>O<sub>3</sub>, with high specific surface (up to 150 m<sup>2</sup>/g), on which the transition metal clusters responsible for the catalytic activity are deposited. There are different kinds of automotive catalysts, like oxidation catalysts, soot particle filters and three-way catalysts (TWC). The oxidation catalysts are designed to completely oxidize carbon monoxide (CO) and hydrocarbons present in the exhaust due to an incomplete combustion in the engine. The soot particle filters are designed to collect (mainly graphitic) carbon particles and to burn them. TWC's owe their name to the fact that they have to abate emissions of three different classes of pollutants: nitrogen oxides NO<sub>x</sub>, CO and hydrocarbons. Differ-

ent catalysts may be combined to achieve the desired effect. For example, Diesel engines must combine an oxidation catalyst with a soot particle filter, since soot is usually not burnt in other catalysts [13], while a gas engine primarily needs an oxidation catalyst [14]. The oxidation catalyst reaches its highest conversion under oxygen-rich conditions. Conversion rates of the chemical species vary when switching from fuel-rich conditions ('rich conditions') to air-rich conditions ('lean conditions');  $\text{NO}_x$ 's are reduced better under rich conditions, while carbon compounds oxidize better under lean conditions. Around stoichiometry there is a region where all conversion rates are rather high (lambda-window), and therefore modern TWC's try to stick to this region by controlling air inlet and fuel injection.

Since temperatures up to  $\sim 800^\circ\text{C}$  are reached during operation, one of the primary concerns is the thermal stability of the catalyst, in particular the tendency of metal clusters to coarsen ('sinter') at high temperatures, either through migration of single atoms (Ostwald ripening) or through migration and fusion of whole clusters (coalescence). Another issue is the worsening of catalytical properties by chemisorption of foreign species (poisoning), above all sulphur and chlorine.

Moreover, the question of the optimal cluster size is of particular importance, since this is a parameter that can be directly controlled during the preparation.

While the cited issues must be systematically addressed to assess the feasibility of an industrial application of new catalysts, it is also important to start analyzing each component of the system independently to gain insight into its role. This thesis is focused on oxide formation on unsupported platinum catalysts under ideal oxygen-rich conditions in the absence of poisoning species and its role in the oxidation of both methane and CO. In particular we will also report results for the stability of platinum oxide clusters in dependence of cluster size.

## 2.2 Mechanisms of heterogeneous catalytic oxidation

A catalyst was defined by J. J. Berzelius in 1836 as a compound which increases the rate of a chemical reaction, but is not consumed by the reaction. The catalyst affects only the rate of the reaction, it changes neither the thermodynamics of the reaction nor the equilibrium composition. The catalysis can be homogeneous, if the catalyst is in the same physical state (liquid/gas) as the reactants, or heterogeneous. Automotive exhaust treatment systems rely on solid state catalysts, i.e. they are based on heterogeneous catalysis. In the case of oxidation reactions of carbon compounds, the overall process consists of dissociation of oxygen molecules, in case dissociation of the carbon-containing molecule and subsequent reaction of the radicals with oxygen to form the products. In heterogeneous catalysis, all these steps occur at the catalyst's surface. Different reaction mechanisms are possible [12], depending on the kind of interaction between reactants and surface and the kind of interaction between reactants. There are three main mechanisms: the Eley-Rideal mechanism, the Langmuir-Hinshelwood mechanism and the Mars-Van Krevelen mechanism.

In the Eley-Rideal mechanism, one adsorbed species reacts with a second species coming directly from the gas phase, without adsorbing (see fig. 2.1(a)). This can occur when, for example, a CO molecule reacts with an oxygen atom adsorbed on the metal surface and the resulting CO<sub>2</sub> is readily released into the gas phase.

In the Langmuir-Hinshelwood mechanism both the oxygen and the carbon species adsorb on the surface of the catalyst, and the product formation occurs through reaction between adsorbate species (see fig. 2.1(b)). Adsorption can be on a single type of surface site or each adsorbing species can adsorb on its type of surface site. A characteristic feature of the system with a single type of surface site is the appearance of a maximum in conversion rate in experiments where the partial pressure of one reactant is increased as the partial pressure of the second reactant is held constant. This phenomenon is associated with the inhibition of the adsorption of one reactant by too high partial pressure of the second reactant. The strong non-linearity of rate equations, which is an expression of the competition of the two species for adsorption, can lead to spectacular effects, e.g. chaotic

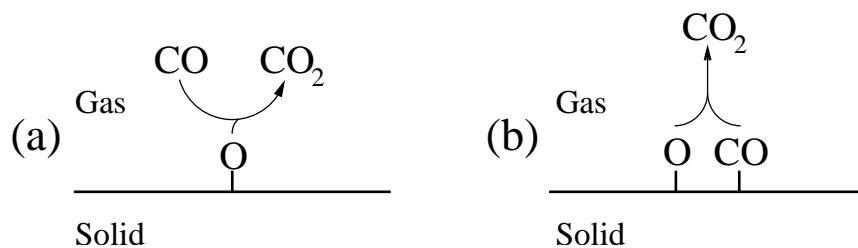


Figure 2.1: (a) The Eley-Rideal mechanism for CO oxidation, with the CO molecule reacting without adsorbing; (b) the Langmuir-Hinshelwood mechanism for CO oxidation, with co-adsorption of the reacting species.

spatio-temporal behaviour in the case of CO oxidation on Pt(110) at low pressures [15]. In these two mechanisms the reacting species only adsorb on the surface of the catalyst and the latter is not further modified.

A third mechanism, the Mars-Van Krevelen, is given when the oxygen does not only chemisorb on the surface of the catalyst, but it reacts with it to form a surface oxide. The carbon species to be oxidized adsorbs on the surface of the oxide, and oxidizes by extracting oxygen atoms from the oxide lattice, thereby reducing the metal oxide, which is subsequently reoxidized by gaseous oxygen (see fig. 2.2). This mechanism has been observed at high oxygen pressures on ruthenium [16], palladium and also in STM experiments on Pt(110) [8]. This last case is described more in detail in the next section.

Occurrence of one mechanism or the other depends not only on the carbon compounds and on the catalyst metal, but also on the conditions under which the reaction occurs: on Pt(110) a switch from adsorbed oxygen to oxide formation at increasing  $O_2/CO$  partial pressure ratio has been observed [8]. This study focuses on oxide formation on platinum catalysts under oxygen-rich conditions and its role in oxidation of both methane and CO.

## 2.3 Platinum as oxidation catalyst

Michael Faraday demonstrated the ability of platinum to bring about the recombination of hydrogen and oxygen. Although the properties of platinum as oxidation catalyst have

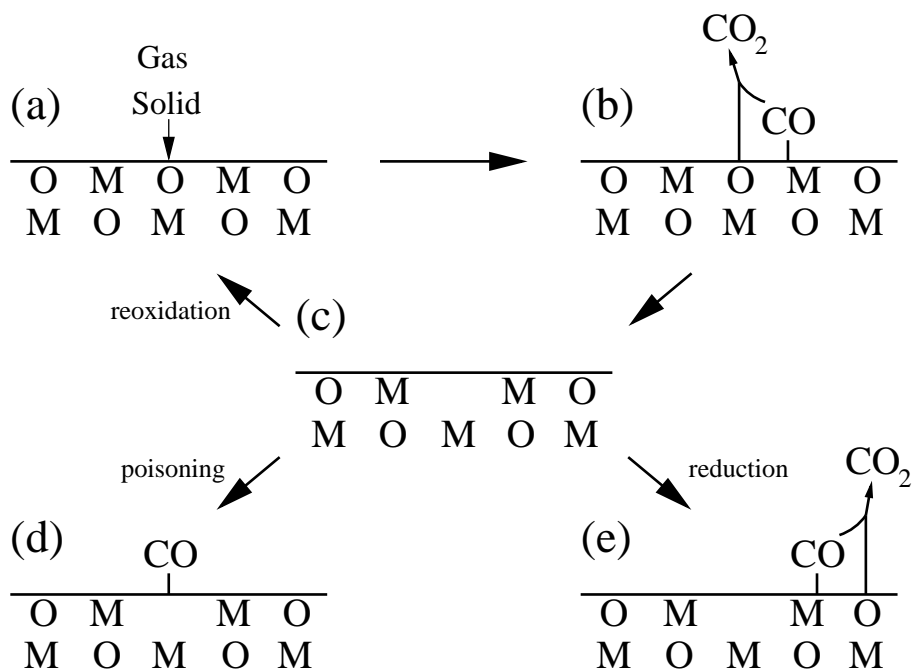


Figure 2.2: (a-c) The Mars-Van Krevelen mechanism for CO oxidation; (a) the oxidized state of the surface (M metal atom, O oxygen atom); (b) oxidation of a CO molecule by an O atom of the oxide lattice, which leads to a partially reduced state of the oxide surface (c). The surface is then brought back to the initial fully oxidized state (a) by reaction with gaseous oxygen and the catalytic cycle is closed. Catalysis through the Mars-Van Krevelen mechanism cannot be sustained if e.g. the reoxidation of the partially reduced state of the oxide surface is hindered by adsorption of CO in the O-vacancies, leading to poisoning (d) or if further reduction of the partially reduced surface through CO is favoured, leading to a metallic surface (e).

been investigated already by Langmuir [17] almost a century ago, the precise nature of the catalytically active sites is still the subject of intense investigation efforts. An oxide layer is thought to form on the surface of the Pt clusters of a car catalyst under oxygen-rich conditions, and the total oxidation of hydrocarbons most probably follows a Mars-Van Krevelen reaction mechanism (see previous section). This hypothesis has been put forward a decade ago by Mallens et al. [18] after a series of carefully conducted experiments of methane oxidation on platinum gauzes at about 1000 K. In more recent years Hendriksen and Frenken [8] investigated the temporal evolution of a Pt(110) surface *in situ* during the catalytic combustion of CO in a high-pressure flow reactor coupled to a scanning tunneling microscope. These authors found that a sudden increase in the catalytic activity of the surface is associated with a dramatic change in its morphology, which was attributed to the formation of a superficial oxide layer. The atomic structure of this layer has only recently been investigated [9, 19], while very little is experimentally known about the structural details of thin oxide layers grown on (100) and (111) Pt surfaces, or on their catalytic oxidation activity. Ertl and co-workers [15] worked on the same systems under ultra-high vacuum (UHV), with partial pressures of oxygen up to  $10^{-3}$  mbar. They identified spatio-temporal pattern formation and non-linear oscillations and explained them in term of non-linearity of the equations that describe the competition for adsorption of the two chemical species in the frame of a Langmuir-Hinshelwood mechanism. This is to be compared with the experiment of Hendriksen and Frenken, and it shows what we discussed in general terms in the previous section: there is a switch from a Langmuir-Hinshelwood mechanism with reaction between adsorbed species at low oxygen pressures to a Mars-Van Krevelen mechanism at high oxygen pressures. In this work we investigate the structures of platinum oxide layers grown on (100) and (111) Pt surfaces, and probe their activity towards the dissociative adsorption of methane and the oxidation of CO via a combination of First-Principles Atomistic Thermodynamics and First-Principles Molecular Dynamics (FPMD) techniques based on Density Functional Theory (DFT).

In general, the catalytic activity of thin oxide layers on transition metals is the result of a delicate dynamical equilibrium between reactants and products, and the availability of suit-



able reactive sites. This leads to reaction channels which are active only in a narrow range of temperatures and oxygen pressures, at equilibrium conditions which may be reached on a time scale of seconds, and may be dominated by kinetic effects [6]. An automobile catalyst is a very complex system whose working state is difficult to define [12], whose features vary with different crystallographic orientation of the metal crystallites, and whose activity may be heavily influenced by the ceramic support [12]. Furthermore, at very high temperatures the decomposition of the oxide layer and the formation of volatile oxide species cannot be excluded [20]. This makes the experimental investigation of the catalytic mechanisms active on the surface of Pt particles difficult to perform at the atomic scale. Therefore atomistic modelling is routinely used nowadays to investigate the relative thermodynamic stabilities of different oxide layers on metallic surfaces at the pressure and temperature conditions typical of catalytic applications [4]. In particular, the recent developments of so-called first-principles atomistic thermodynamics techniques have led to the characterisation of many surface oxide structures on a variety of transition metal surfaces [6]. Notably, thermodynamically stable ultrathin oxide layers can be non-commensurate with respect to the underlying substrate, non-stoichiometric, and can present structures which reflect the short-range ordering of the bulk phases in typical coordination motifs around the metal ions, but do not have the same long-range order [21].

Commonly formed platinum oxide structures comprise PtO, Pt<sub>3</sub>O<sub>4</sub>,  $\alpha$ -PtO<sub>2</sub>, and  $\beta$ -PtO<sub>2</sub> [22, 23]. As reported by Muller and Roy,  $\alpha$ -PtO<sub>2</sub> is the thermodynamically stable bulk phase at low temperatures and low oxygen pressures. At higher temperatures, the formation of Pt<sub>3</sub>O<sub>4</sub> becomes more favourable, while the PtO phase has been observed not to be stable in any interval of temperature and pressure. The  $\beta$ -PtO<sub>2</sub> phase becomes stable only at oxygen partial pressures of several hundreds atmospheres. Similar results were reported by Punnoose and co-workers, who examined the oxidation state of supported Pt clusters in air [24] at increasing temperatures. These authors found the occurrence of two phase transitions near 910 K and 1070 K, and related them to the transitions  $\alpha$ -PtO<sub>2</sub>  $\rightarrow$  Pt<sub>3</sub>O<sub>4</sub>  $\rightarrow$  Pt. Finally, nanoscopic platinum clusters were observed to fully oxidize after two hours treatment at 770 K at nearly atmospheric air pressures, and a strong dependence of the oxidation

state on cluster size has been established [25]. There are two main proposals for the crystal structure of  $\text{Pt}_3\text{O}_4$ : while Galloni and Roffo [26] had proposed a body-centered cubic (BCC) structure to explain X-ray data, Muller and Roy [22] argued that a simple cubic (SC) structure would better explain the experimental data.

As far as theoretical calculations are concerned, Tang and co-workers [27] have produced a phase diagram of oxygen adsorbed on Pt(111) up to half monolayer coverage by using first-principles methods. Li et al. [9] investigated the initial oxide formation on Pt(110) by using a combination of experimental and first-principles techniques, and suggested the formed phase to be  $\text{PtO}_2$ . Later, Li and Hammer [10] proposed that  $\alpha$ - $\text{PtO}_2$  submonolayers could form on Pt(111) and showed with DFT calculations that three-phase boundaries involving these structures could lower the barrier for CO oxidation in comparison to a metallic surface. Moreover, the oxidation of CO on  $\beta$ - $\text{PtO}_2$  has been recently investigated by Gong et al. [28] and was found to take place through a reaction involving molecular oxygen. It has been clearly established that some Pt oxide structures form under conditions relevant for catalysis. However, in the currently available literature there is no systematic study that links the formation of a well defined platinum oxide structure to its catalytic activity towards methane oxidation, while only few, recent studies focused on the oxidation of CO on Pt(110) and Pt(111). In particular, the formation of oxide films on Pt(100), a surface that is known to be normally present in platinum clusters [11], has been overlooked so far. We present here results of an investigation of platinum oxides under oxygen-rich conditions through Density Functional Theory (DFT), First-Principles Molecular Dynamics (FPMD) and First-Principles Atomistic Thermodynamics. Phase diagrams for bulk oxides and for oxide clusters have been calculated, oxidation of Pt surfaces and formation of oxide films has been investigated, and adsorption of methane and CO on relevant structures has been simulated. We have individuated the oxide phase with the most convenient adsorption properties and discussed its existence in bulk and clusters.

The computational techniques and the simulation parameters are described in the next chapter. Results on the thermodynamics of oxides are reported in chapter 4 and those on the catalytic reactions in chapter 5. Finally, conclusions are drawn in chapter 6.

# Chapter 3

## Computational Methods

We have performed electronic and structural optimizations as well as First-Principles Molecular Dynamics (FPMD) [29, 30] using the Car-Parrinello (CP) method [31] and spin-paired Density Functional Theory (DFT) [32, 33] within the PW91 Generalized Gradient Approximation (GGA) [34], as implemented in the LAUTREC code [35, 36].

Density Functional Theory (DFT) reduces the problem of many interacting electrons to a problem of non-interacting electrons in an effective potential, making possible the calculation of the electronic structure of systems with many atoms. The atomic motion is simulated with the Car-Parrinello molecular dynamics approach, where the electronic states undergo a fictitious dynamics to follow the classical newtonian motion of the nuclei. To compare the thermodynamic stability of different phases at constant temperature and pressure, we need to compute Gibbs' free energies. In order to do this, the contributions of the lattice vibrations of solid phases to enthalpy and entropy need to be calculated. The quasiparticles obtained through quantization of these oscillations are called phonons. The sum of the total DFT energy and the contribution of the phonons to the Gibbs' free energy determinate the Gibbs' free energy of the bulk phase. Relative stability of two phases is then determined by the difference of their Gibbs' free energies.

## 3.1 Fundamentals of Density Functional Theory

When tackling a dynamical simulation involving nuclei and ions, a first simplification is to separate the problems of determining the ground state of the electrons from that of determining the forces on the ions. Through the methods described in the next subsection it is possible to substitute the original problem of interacting electrons and nuclei with two separate problems: (i) the dynamics of interacting electrons in the field of static nuclei; (ii) the 'dressed' dynamics of the nuclei interacting through an effective interaction.

### 3.1.1 Adiabatic approximation

We work with systems which can be described by the Schrödinger equation. The temporal evolution of the system is described by:

$$H(R_n, r_n, t)\Phi(R_n, r_n, t) = i\hbar \frac{\delta\Phi(R_n, r_n, t)}{\delta t} \quad (3.1)$$

where  $H$  is the Hamiltonian of the whole system,  $\Phi$  the wavefunction, the  $R_n$ 's are the coordinates of the nuclei and the  $r_n$ 's the coordinates of the electrons. If the system evolves in a way, so that no energy exchange between electrons and nuclei takes place, then the dynamics of nuclei and that of electrons can be handled separately according to the adiabatic approximation [37]. The use of this approximation is made possible by the fact that nuclei have a much larger mass than the electrons (at least 1836.15 times heavier). The adiabatic approximation is the formalization of the intuitive idea that electrons almost instantaneously adapt to the positions of the nuclei, and that their wave functions change smoothly, when nuclei move. As a consequence, the electrons can be considered always in the ground state corresponding to the instantaneous position of the nuclei. At a given fixed position of the nuclei the stationary Schrödinger equation is:

$$H(R_n, r_n)\Psi(r_n) = E_0(R_n)\Psi(r_n) \quad (3.2)$$

The solution of this equation leads to the ground state energy  $E_0$ , which defines the potential acting on the nuclei.  $E_0$  can then be introduced in the equation for the nuclei, either

the Schrödinger equation or the classical newtonian equation:

$$M_I \frac{d^2 R_I}{dt^2} = - \frac{dE_0(R_n)}{dR_I} \quad (3.3)$$

A quantum description of the motion of the ions is sometimes necessary, as e.g. in the case of tunneling processes. Otherwise one can treat nuclei as classical particles, as it is done in this thesis. Forces on the atoms are calculated as quantum mechanical expectation values of the spatial derivatives of the Hamiltonian via the theorem of Hellmann-Feynman.

### 3.1.2 Theorems of Hohenberg and Kohn

The problem of the determination of the electronic structure of the system has been reduced to finding the solution of a stationary Schrödinger equation. Anyway solving the Schrödinger equation for N interacting electrons is a formidable task, and it needs further simplification to be handled in an effective way. The density functional theory (DFT) reduces the problem of many interacting electrons to a problem of independent electrons in an effective potential. In this way the dimensionality of the problem is reduced from the original  $3*N$  space variables (N number of electrons) to 3.

The DFT is based on the theorems of Hohenberg and Kohn [32] and on the Kohn-Sham equations [33]. The theorems of Hohenberg and Kohn have general validity for a many-particle system with arbitrary interaction and in particular for the electron gas with Coulomb interaction in an external potential originating from the atomic nuclei. Starting from the separation of the total energy

$$H = T + U + V_{ext} \quad (3.4)$$

in kinetic energy T, interaction of the particles among themselves U and contribution from the external potential  $V_{ext}$  ( $V_{ext} = \int v_{ext}(r)n(r)dr$ ), the theorems of Hohenberg and Kohn state that:

1) All ground state properties of a sytem are univocal functionals of the ground state density  $n_0$  of the system. It is clear that all expectation values are univocal functionals of the given external potential  $V_{ext}(r)$  (expectation values are calculated from wave functions

that are solutions of the Schrödinger equation and are therefore determined by  $V_{ext}(r)$ ). In particular this is true for the electron density. The central statement is that the reverse is also true: given a density  $n$ , there exists a unique external potential  $V_{ext}$  (up to a constant) for which  $n(r)$  can be calculated from the solution of the Schrödinger equation.  $V_{ext}$  is an univocal functional of the electron density, which means  $V_{ext} = V_{ext}[n]$ . Through  $V_{ext}$  all ground state properties are then determined, in particular also the ground state energy  $E_0$ .

2) The total energy functional  $E[n]$  of a system with  $N$  electrons obeys a variational principle, i.e.  $E[n]$  is minimized by the ground state density  $n_0$ .

While the first theorem is the formal justification for working with the density  $n$  instead of the total wavefunction, the second makes it possible to find the ground state density through variation of the energy functional of the density.

### 3.1.3 Kohn-Sham equations

The functional  $E[n]$  still has the complexity of the initial many-body problem through the term  $U$ , and it is unknown. On the other side, for a system of non-interacting particles in an external potential  $v$  we know the functional:

$$V[n] = \int v(r)n(r)dr \quad (3.5)$$

as well as the kinetic and electrostatic functionals:

$$T_0[n] = \langle \Psi | T | \Psi \rangle \quad (3.6)$$

$$E_H[n] = \frac{1}{2} \int \int \frac{n(r)n(r')}{|r-r'|} dr dr' \quad (3.7)$$

where we have expressed everything in atomic units to get rid of constants. If we express the energy functional of interacting electrons in term of these previous quantities, there is a remaining part that defines the exchange-correlation energy term:

$$E_{xc}[n] = E[n] - T_0[n] - E_H[n] \quad (3.8)$$

The total energy can be then re-written as:

$$E_0 = \min_n [T_0[n] + V[n] + E_H[n] + E_{xc}[n]] = \min_n [T_0[n] + V_{KS}[n]] \quad (3.9)$$

where the Kohn-Sham functional  $V_{KS}$  has been defined.

It is easy to recognize that a system of *non*-interacting electrons in a *fictitious* Kohn-Sham potential obeys the same minimum-principle, where the potential is:

$$v_{KS}(r) = v(r) + \int \frac{n(r')}{|r - r'|} dr' + \frac{\delta E_{xc}[n(r)]}{\delta n(r)} \quad (3.10)$$

where the last term is the exchange-correlation potential.

By this method a single problem with  $N$  interacting electrons can be mapped into  $N$  problems with non-interacting electrons, the so-called Kohn-Sham equations:

$$\left(-\frac{1}{2}\nabla^2 + v_{KS}(r)\right)\psi_i(r) = \epsilon_i\psi_i(r) \quad (3.11)$$

which can be solved selfconsistently, as far as the exchange-correlation potential is known. The wavefunctions  $\psi_i$  are the single-particle Kohn-Sham orbitals, from which the density can be calculated as:

$$n(r) = \sum_i \psi_i^*(r)\psi_i(r) \quad (3.12)$$

The exchange-correlation potential is not known in closed form, but there are approximate formulae for it which are fitted to Quantum Monte Carlo data for the electron gas [38]. These formulae are obtained within certain approximations; the most popular are the Local Density Approximation (LDA), which is based on the hypothesis that the local exchange-correlation contribution to the energy is a function only of the electron density in that point, and the Generalized Gradient Approximation (GGA), which writes the local exchange-correlation contribution to the energy as a function of the density in that point and its derivatives with respect to space coordinates. In the present work the exchange-correlation energy and potentials have been calculated within GGA in the formulation by Perdew and Wang (PW91 [34]), with exception of the phonon calculations, in which the formulation by Perdew, Burke and Ernzerhof (PBE [39]) has been used.

Since only valence electrons participate in bond-forming and therefore change according to the environment the atom finds itself in, while core wavefunctions remain unchanged, only valence electrons are explicitly calculated, and the interaction of these with core electrons is dealt with by introducing a pseudopotential which mimics this interaction. We have used

Troulliers-Martin norm-conserving pseudopotentials [40], with exception of the GGA+U calculations (see section 3.1.7), in which Vanderbilt ultrasoft pseudopotentials have been employed [41].

## 3.2 Ab-initio molecular dynamics

An efficient scheme for the calculation of the electronic ground state and for the Molecular Dynamics (MD) simulation is the Car-Parrinello method [31]. In this method the wavefunctions evolve according to a fictitious classical newtonian dynamics with a fictitious electron mass:

$$\mu \frac{d^2 \psi_i}{dt^2} = -H \psi_i - \eta \frac{d\psi_i}{dt} + \sum_j \Lambda_{ij} \psi_j \quad (3.13)$$

where the friction coefficient  $\eta$  is empirically chosen to damp critically the electron motion to search for ground state and the Lagrange multipliers  $\Lambda_{ij}$  have been introduced to have the orthonormality of the wavefunctions conserved. A Lagrangian for the whole system can then be written:

$$L = \sum_I \frac{1}{2} M_I \frac{dR_I}{dt}^2 + \sum_i \mu \langle \psi_i | \psi_i \rangle - E[\psi, R] + \sum_{ij} \Lambda_{ij} (\langle \psi_i | \psi_j \rangle - \delta_{ij}) \quad (3.14)$$

so that electrons and nuclei can be dealt with on the same level:

$$\mu \frac{d^2 \psi}{dt^2} = -H \psi + \sum_j \Lambda_{ij} \psi_j \quad (3.15)$$

$$M_I \frac{d^2 R_I}{dt^2} = -\frac{dE_{tot}}{dR_I} \quad (3.16)$$

Both sets of equations can then be solved simultaneously, e.g. by using the Verlet algorithm.

## 3.3 Ab-initio thermodynamics

In the previous sections we have shown how to calculate the ground state energy of a system composed of electrons and nuclei through the DFT. On the other hand we are interested in predicting the relative thermodynamic stability of platinum and its oxides



PtO<sub>x</sub> in a system at constant temperature and pressure. At temperatures higher than zero the relevant quantity that determines relative stability of different phases is not the total energy, but the free energy. Since most technologically relevant catalytic processes work at high temperature and at atmospheric pressure, it is necessary to take into account the effects of pressure  $p$  and temperature  $T$  on the relative stability of different phases. In the following we will start from the hypothesis that the system has a constant pressure, and therefore the relevant free energy is the Gibbs' free energy. The stable phase at a certain  $(T,p)$  corresponds to the minimum Gibbs' free energy. The theory described below is specifically designed for the case that the two phases to be compared are the pure metal Pt and a metal oxide PtO<sub>x</sub>. The system is in thermodynamic equilibrium with a reservoir of oxygen gas and mass transport takes place between system and reservoir.

We write the Gibbs' free energy as:

$$G(T, p, N_{Pt}, N_O) = F - TS = E + pV - TS \quad (3.17)$$

where  $F$  is Helmholtz's free energy,  $S$  the entropy,  $E$  the energy and  $V$  the volume. Since we consider solid state phases, the term  $pV$  may be safely overlooked [5]. In particular the Gibbs' free energy of formation of an oxide phase PtO<sub>x</sub> from metal and oxygen gas can be written as:

$$\Delta G_f^{PtO_x} = G_{PtO_x} - G_{Pt} - \frac{x}{2}G_{O_2} \quad (3.18)$$

$F$  and  $S$  for the oxygen gas are taken from thermodynamic tables [42].

We have also studied the oxidation of metallic surfaces, modelled as slabs with periodic boundary conditions. The theory can be easily adapted to the calculation of surface free energies:

$$\gamma(T, p) = \frac{1}{A_{tot}}[G(T, p, N_{Pt}, N_O) - N_{Pt}\mu_{Pt}(T, p) - N_O\mu_O(T, p)] \quad (3.19)$$

where  $\mu_{Pt}$  and  $\mu_O$  are the chemical potentials of Pt and O respectively, and  $A_{tot}$  is the total surface area. The semi-infinite crystal under the surface represents a reservoir for platinum atoms, and the gas a reservoir of oxygen. In the case that the inner of the crystal is an oxide PtO<sub>x</sub>, it is a reservoir for both platinum atoms and oxygen, and the chemical

potentials of the two elements are connected through the free energy of the oxide:

$$\mu_{Pt}(T, p) + x\mu_O(T, p) = g_{PtO_x}^{bulk}(T, p) \quad (3.20)$$

where the small  $g$  denotes the Gibbs' free energy per formula unit, so that the previous equation becomes:

$$\gamma(T, p) = \frac{1}{A_{tot}} [G(T, p, N_{Pt}, N_O) - N_{Pt}g_{PtO_x}^{bulk}(T, p) + (xN_{Pt} - N_O)\mu_O(T, p)] \quad (3.21)$$

All quantities in this expression can be calculated with DFT or obtained from thermodynamic tables.

The energy of the oxygen molecule at  $T=0$  K,  $p=0$  atm has been calculated with spin-polarized DFT.

### 3.4 Phonons

Atom vibrations around the equilibrium positions in a solid phase, i.e. the phonons of the crystal, contribute to the Gibbs' free energy of the system. These contributions can be calculated in the frame of Density Functional Perturbation Theory (DFPT) [43, 44, 45]. This allows calculations of phonon frequencies, which can be used to calculate thermodynamic quantities within the harmonic approximation [46].

Let's consider a system in its ground state, for which the Kohn-Sham potential  $V_{SCF}$  and the ground state electron density  $n_0$  have been calculated in selfconsistent way. The atoms are then displaced from their equilibrium position  $\mathbf{R}$  by a periodic displacement  $u_{\alpha i}(\mathbf{R})$  ( $\alpha$  index of displacement,  $i$  space coordinate), where

$$u_{\alpha i}(\mathbf{R}) = u_{\alpha i \mathbf{q}} e^{i\mathbf{q} \cdot \mathbf{R}} \quad (3.22)$$

The perturbed system has a new electronic ground state, and the new selfconsistent Kohn-Sham potential and the new density differ from the original ones by  $\Delta V_{SCF}$  and  $\Delta n$  respectively. If  $\Delta V_{SCF}$  is known, then  $\Delta n$  can be calculated by first-order perturbation theory through [43]

$$\Delta n(\mathbf{q} + \mathbf{G}) = \frac{4}{N\Omega} \sum_{\mathbf{k}} \sum_{\nu} \langle \psi_{\nu, \mathbf{k}} | \exp(-i(\mathbf{q} + \mathbf{G}) \cdot \mathbf{r}) P_c | \Delta \psi_{\nu, \mathbf{k} + \mathbf{q}} \rangle \quad (3.23)$$

where  $P_c$  is the projector on the conduction band,  $\nu$  the band index,  $\Omega$  the volume of the simulation cell,  $\mathbf{G}$  a reciprocal lattice vector and  $\mathbf{k}$  a vector in the first Brillouin zone. The  $\Delta\psi$ 's are solutions of

$$[\epsilon_{\nu,\mathbf{k}} - H_{SCF}] \Delta\psi_{\nu,\mathbf{k}+\mathbf{q}} \rangle = P_c \Delta V_{SCF}^q |\psi_{\nu,\mathbf{k}} \rangle \quad (3.24)$$

On the other hand, if  $\Delta n$  is known,  $\Delta V_{SCF}$  can be calculated by linearizing Eq 3.10:

$$\Delta V_{SCF}(\mathbf{r}) = \Delta V_{ion}(\mathbf{r}) + \int \frac{\Delta n(r')}{|r-r'|} dr' + \Delta n(\mathbf{r}) \frac{dv_{xc}}{dn} \Big|_{n=n_0(\mathbf{r})} \quad (3.25)$$

Eq. 3.24 and eq. 3.25 are a system for the selfconsistent calculation of  $\Delta V_{SCF}$  and  $\Delta\psi$ . From the calculation of the response, the matrix of force constants can be calculated, from which phonon frequencies are derived. The matrix of force constants is:

$$C_{\alpha i, \beta j}(\mathbf{R} - \mathbf{R}') = \frac{\partial^2 E}{\partial u_{\alpha i}(\mathbf{R}) \partial u_{\beta j}(\mathbf{R}')} = C_{\alpha i, \beta j}^{ion}(\mathbf{R} - \mathbf{R}') + C_{\alpha i, \beta j}^{elec}(\mathbf{R} - \mathbf{R}') \quad (3.26)$$

where  $C^{ion}$  is the contribution of the ions to the force constants.  $C^{elec}$  is:

$$C_{\alpha i, \beta j}^{elec}(\mathbf{R} - \mathbf{R}') = \int \left( \frac{\partial n(\mathbf{r})}{\partial u_{\alpha i}(\mathbf{R})} \frac{\partial V_{ion}(\mathbf{r})}{\partial u_{\beta j}(\mathbf{R}')} + n_0(\mathbf{r}) \frac{\partial^2 V_{ion}(\mathbf{r})}{\partial u_{\alpha i}(\mathbf{R}) \partial u_{\beta j}(\mathbf{R}')} \right) d\mathbf{r} \quad (3.27)$$

Phonon frequencies are then obtained by diagonalization of the dynamical matrix. The theory must be slightly adapted in case of polarizable isolators, because in such crystals a macroscopic electric field is created by an ion displacement with  $\mathbf{k} = 0$  (center of the Brillouin zone), which must be handled separately:

$$C_{\alpha i, \beta j} = C_{\alpha i, \beta j}^{an} + C_{\alpha i, \beta j}^{na} \quad (3.28)$$

where  $C^{an}$  is the analytical part (eq. 3.26) and  $C^{na}$  is the non-analytical part; the non-analytical part of the force matrix due to the macroscopic electric field has the general form:

$$C_{\alpha i, \beta j}^{na} = \frac{4\pi}{\Omega} \frac{(\mathbf{q} \cdot \mathbf{Z}_i^*)_{\alpha} (\mathbf{q} \cdot \mathbf{Z}_j^*)_{\beta}}{\mathbf{q} \cdot \epsilon^{\infty} \cdot \mathbf{q}} \quad (3.29)$$

where  $\Omega$  is the cell volume and  $\epsilon^{\infty}$  is the high-frequency dielectric tensor which is defined by the relation between external applied electric field  $\mathbf{E}_0$  and total electric field  $\mathbf{E}$ :  $\mathbf{E}_0 = \epsilon^{\infty} \mathbf{E}$ ;  $\mathbf{Z}_{i,\alpha\beta}^*$  are the Born effective charges:

$$\mathbf{Z}_{i,\alpha\beta}^* = \Omega \frac{\partial P_{\alpha}^{tot}}{\partial u_{\beta,i,\mathbf{q}=0}} \quad (3.30)$$

where  $P^{tot}$  is the total polarization of the cell and the  $u$ 's are the atomic displacements. So the Born effective charge is linked to a change in the total polarization due to an ion displacement.

Care must be used when trying to interpret physically the meaning of the Born electric charges. Since they are dynamical charges, i.e. they are a measure of the response to a perturbation, their relation with the oxidation state of the ion is non-trivial, unless the bonds in the solid are purely ionic. Born effective charges can be interpreted as arising from two contributions: the polarization change due to the rigid displacement of the ionic charges plus a dynamical contribution. The latter may be due in principle either to local polarizability or to charge transfer between ions induced by the ion displacement [47]. When a material is partly covalent and partly ionic, the dynamical charges can be very different from their nominal values: the displacement of an ion induces a non-rigid displacement of the associated electronic charge [48]. In particular it was shown that in the case of  $\text{KNbO}_3$  an anomalous value of Born effective charges arises only in presence of covalent bonding [49], and that, at least in  $\text{ABO}_3$  compounds, the dynamical contribution comes from a transfer of charges rather than from local polarizability [47]. Also connections to the electronic structure was investigated, and it was shown that the change of polarization due to the displacement of an ion can be put directly in connection with a displacement of the centers of the Wannier functions [50].

### 3.5 GGA+U

There are a few systems for which the usual LDA and GGA approximations to the DFT even in the spin-polarized versions fail to predict the correct ground state. Best known cases are magnetic oxides of the 3d transition metals, like NiO [51] and FeO [52]; for example in the case of FeO conventional Local Spin Density Approximation (LSDA) approaches predict a metallic ground state, while the ground state is experimentally known to be an insulator [52]. The reason of these failures has been found to be the inability of these simple DFT schemes to take into account the strong interactions (strong on site Coulomb

repulsion) between very localized d-states [53, 54]. A solution to this shortcoming is to add a term into the Hamiltonian which takes explicitly into account these interactions. This approach is called LDA+U or GGA+U, according to the approximation used for exchange and correlation; the Hamiltonian of the system can be written in slightly different forms, one of which is [52]:

$$E = E_{LDA} + \sum_I \left[ \frac{U}{2} \sum_{m, \sigma \neq m', \sigma'} n_m^{I\sigma} n_{m'}^{I\sigma'} - \frac{U}{2} n^I (n^I - 1) \right] \quad (3.31)$$

where  $n$  is the atomic orbital occupation,  $I$  the atom,  $m$  the orbital,  $\sigma$  the spin,  $n_m^{I\sigma} = n_{mm}^{I\sigma}$ ,  $n^I = \sum_{m, \sigma} n_m^{I\sigma}$ . The  $U$  term (Hubbard term) mimics the strong correlation between d-electrons and the interaction is designed to favour integer occupation numbers of the d-orbitals. In particular in the above mentioned FeO it forces an energy splitting between the spin-up and spin-down orbitals, with the result that, instead of having up- and down-states with equal fractional occupation, the system evolves to a Mott insulator with a full band of one spin and an empty band of the other spin separated by a clear gap, in agreement with experimental results.

Since for two Pt oxides we have found a metallic ground state, we have performed a series of calculations with GGA+U with the Quantum-ESPRESSO package [55] to test if an insulating state could be obtained by choosing a non-zero  $U$  and at the same time to check whether our adsorption energies on the surfaces of these oxides are strongly influenced by the position of the d-bands in the metal ions.

Although it is in principle possible to calculate the factor  $U$  in a selfconsistent way [52], this does not assure a better adherence to experimental results in case of systems that are not strongly correlated such as TiO [53]. For this oxide LDA+U with  $U$  calculated from LDA incorrectly leads to antiferromagnetic insulators rather than a paramagnetic metal. Therefore we have chosen reasonable values of between 4 and 15 eV to see how strongly the results deviate from those of the simple spin-paired DFT-GGA when the d-bands are shifted, without pursuing a selfconsistent treatment.

## 3.6 Bader charges

In a solid or a molecule there is no univocal method to assign electronic charge distributed in space to a certain ion. One popular way to do so is the Bader's 'Ion in Molecule' approach [56]. This is a method that uses geometrical features of charge density to divide space into atom basins around each ion. The charge present in the basin is assigned to the ion. In contrast to the Born effective charges considered in the subsection 3.4, which are dynamical charges, i.e. they are a measure of the response to a perturbation, the Bader charges are static charges, i.e. they describe a property of the electronic charge distribution, and help characterizing the charge distribution in a compound.

To determine the external surface of the basin, points with a zero gradient of the density need to be determined. These can be classified according to the eigenvalues of the Hessian matrix (the matrix of the second partial derivatives with respect to the spatial coordinates) of the charge density in bonding, ring and cage critical points (see also fig. 3.1).

Bonding critical points of the Bader surface are those that have one positive eigenvalue and two negative. These belong to a face of the Bader volume and are used to separate the basins of the two atoms: the charge that lies between this minimum and an atom is assigned to this atom. Ring critical points have two positive eigenvalues and one negative, and belong to an edge of the Bader volume. Cage critical points are a global minimum of the electron density and define a vertex of the Bader volume.

From the Bader charges one gets useful information about the amount of charge transfer between Pt and O in an oxide, and therefore about the real oxidation state of Pt. Inspection of Laplacian of the density at the critical point between two atoms gives qualitative information about the nature of the bond: a negative value of the Laplacian indicates a bond with a high degree of covalency, a zero Laplacian with a small value of the density rather indicates a bond with mostly ionic character.

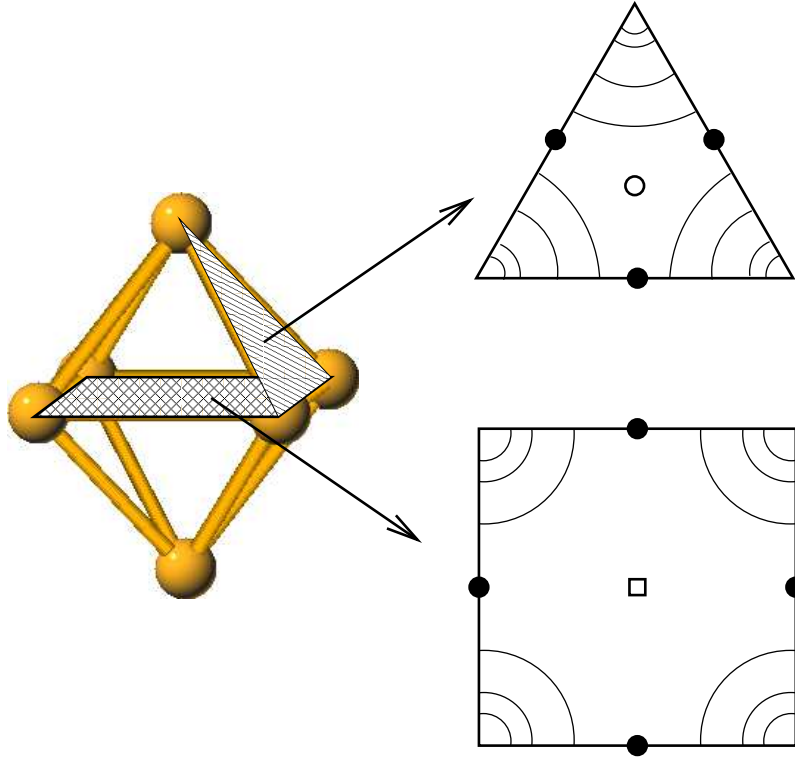


Figure 3.1: Critical points of the charge density; the vertices of the big square and of the triangle are occupied by atoms, the arcs are isodensity lines (contour map of the electronic density). Full circles: bonding critical points; void circle: ring critical point; square: cage critical point (local minimum of the charge density).

### 3.7 Calculation details

Molecular dynamics simulations and total energy calculations have been performed with the LAUTREC code [35, 36]. Periodic boundary conditions and plane waves with an energy cutoff of 50 Rydberg (Ry) to 70 Ry have been used, together with separable norm-conserving Troullier-Martins pseudopotentials [40] already tested in previous works [57]. Special k-points for integration in the first Brillouin zone have been produced with the method of Monkhorst and Pack [58] and checked for convergence. For example for bulk Pt with a 6X6X6 mesh (28 k-points) we have obtained an optimized lattice parameter of

3.98 Å (exp. 3.92 Å [59], other DFT-GGA 4.00 Å [60]) and a bulk modulus B of 228 GPa (exp. 228 GPa at 293.15 K [61]). To model the Pt(111) surface a slab with five layers in the 2X2 surface cell with a 1X3X3 k-point mesh (5 k-points) has been used and a surface energy of 103 meV/Å<sup>2</sup> has been obtained, to be compared with another other DFT-GGA calculation, which gave 97 meV/Å<sup>2</sup> [60].

Phonon calculations have been performed within Density Functional Perturbation Theory [43] with the ABINIT package [62], using the conjugate-gradient algorithm of Gonze [44]. Since eigenvalues and derivatives of electronic wavefunctions are more sensitive to parameter variation than structural properties and total energies, they have been calculated with a cutoff of 70 Ry. Reliability of the phonon calculations was assessed by comparing calculated phonon band structure of bulk platinum with available data [63, 64].

The GGA+U calculations have been performed with the Quantum-ESPRESSO package [55] with ultrasoft pseudopotentials [41]. The use of this kind of pseudopotential has made it possible to use a cutoff energy of 40 Ry.



# Chapter 4

## Structure and thermodynamics of platinum oxides

The starting point of our work is the investigation of structure and thermodynamics of platinum oxides, in form of bulk solids, surfaces, ultrathin films and clusters. This first part provides the basic knowledge about oxide structures that may form on a catalyst under the relevant conditions and represents a prerequisite for the study of the catalytic effects of oxide formation.

### 4.1 Bulk platinum oxides

A comprehensive listing of commonly available platinum oxide phases, along with their temperature and pressure stabilities in the 400-900°C temperature and 20-3500 atm pressure ranges has been reported in Ref. [22] (see fig. 4.1). These comprise PtO, Pt<sub>3</sub>O<sub>4</sub>,  $\alpha$ -PtO<sub>2</sub>, and  $\beta$ -PtO<sub>2</sub> [22, 23]. We have optimized the lattice parameters of all platinum phases and calculated their relative thermodynamic stabilities. In fig. 4.2 the crystal structures of the bulk platinum oxides are sketched, in table 4.1 the optimized structural parameters are reported.

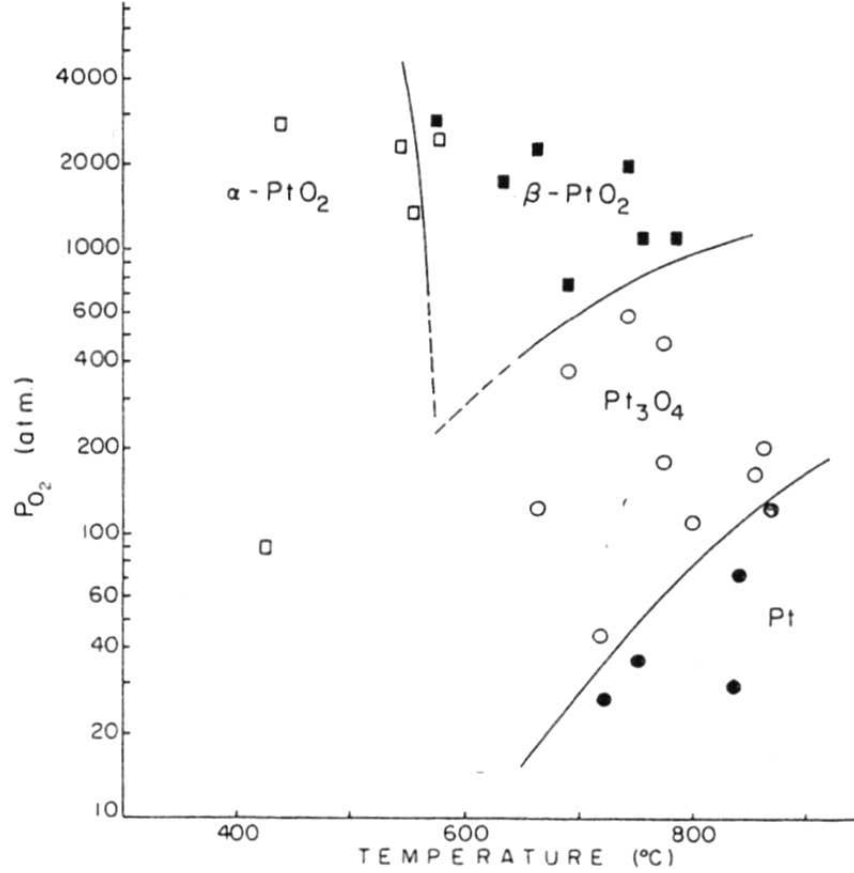


Figure 4.1: Phase diagram for the Pt-O system, as found experimentally by Muller and Roy [22, 66].

#### 4.1.1 $\alpha$ -PtO<sub>2</sub>

$\alpha$ -PtO<sub>2</sub> crystallizes in the hexagonal CdI<sub>2</sub> structure and presents a laminar structure consisting of stacked O-Pt-O trilayers which are covalently bonded in plane, while the interactions between trilayers are of Van der Waals type [10, 22]. While a good agreement between the experimental and computed edge of the hexagonal cell could be achieved (3.10 vs. 3.14 Å), the GGA approximation heavily underestimates the interlayer forces [67], similarly to the case of graphite [68]. The energy versus layer separation curve presents a very shallow minimum (37 meV per Pt atom) corresponding to a  $c/a$  ratio of 1.85 (the reported experimental value is about 1.4 [22]). As a comparison, at the LDA level we obtain a  $c/a$

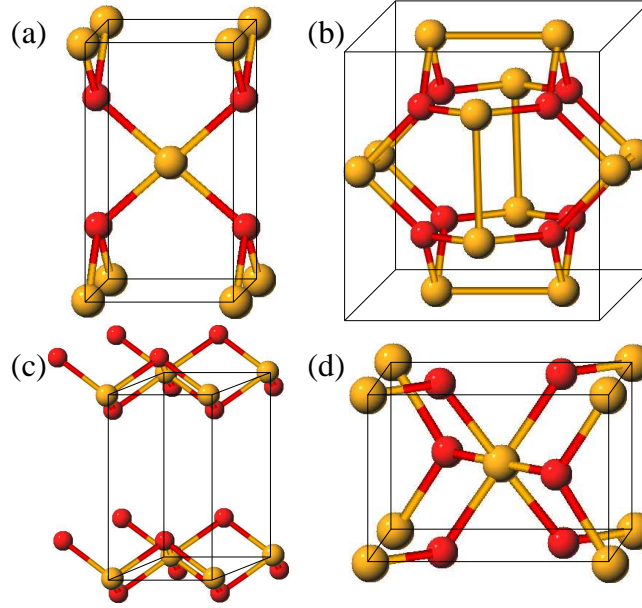


Figure 4.2: Crystal structure of platinum oxides: (a) PtO; (b) Pt<sub>3</sub>O<sub>4</sub>; (c)  $\alpha$ -PtO<sub>2</sub>; (d)  $\beta$ -PtO<sub>2</sub>

value of 1.29 and a larger interlayer binding energy (49 meV per Pt atom). The existence of weak interlayer bonding is consistent with the experimental observation of poor crystallization in the  $c$ -axis direction [22].

As far as electronic properties are concerned, we find an indirect electronic gap of 1.49 eV (see fig. 4.3) within GGA approximation.  $\alpha$ -PtO<sub>2</sub> is experimentally known to be a p-type semiconductor with a gap of 1.84 eV [71]. Such an underestimation of the electronic band gap is typical of DFT-GGA. The top of the valence band is at the  $\Gamma$ -point, while the bottom of the conduction band is on the  $\Gamma$ -M line. The Pt atom has a Bader charge of +1.53 |e|, the oxygens -0.76 |e|; these values, much lower than the nominal charges (+4 and -2 respectively), underline the fact that this transition metal oxide is far from being a purely ionic compound.

This is confirmed also by the calculation of the Born effective charges, which are strongly anisotropic and markedly differ from nominal valence in the direction of the  $c$ -axis. On the contrary, in the other two directions the Born effective charges are equal to the nominal

	PtO <sup>a</sup>	Pt <sub>3</sub> O <sub>4</sub> <sup>b</sup>	$\alpha$ -PtO <sub>2</sub> <sup>b</sup>	$\beta$ -PtO <sub>2</sub> <sup>c</sup>
structure	tetragonal (PdS structure)	simple cubic	hexagonal (CdI <sub>2</sub> structure)	orthorombic (CaCl <sub>2</sub> structure)
a (Å)	3.10 (3.0777)	5.65 (5.585)	3.14 (3.10)	4.49 (4.4839)
b/a	-	-	-	1.05 (1.01)
c/a	1.745 (1.735)	-	1.85 (1.38-1.42)	0.70 (0.70)
Pt-O (Å)	2.06 (2.04)	2.00 (1.974)	2.05	2.03 (1.99)
Pt-Pt (Å)	3.10 (3.0777)	2.83 (2.792)	3.14 (3.10)	3.15 (3.14)
B (GPa)	368	262	-	246 (265 <sup>d</sup> )
E <sub>gap</sub> (eV)	metallic	metallic	1.49 (1.84 <sup>e</sup> )	0.43

Table 4.1: Bulk properties of platinum oxides. B is the bulk modulus, E<sub>gap</sub> the electronic band gap. In parentheses experimental data are reported. <sup>a</sup> Ref. [65]. <sup>b</sup> Ref. [22]. <sup>c</sup> Ref. [69]. <sup>d</sup> Calculated with DFT, Ref. [70]. <sup>e</sup> Ref. [71].

ion charges (4.02 for Pt and -2.01 for O) and the dielectric tensor components ( $\epsilon_{22} = 7.67$ ) are rather typical of a semiconductor (e.g.  $\epsilon = 11$  for GaAs). In a purely ionic crystal with charges rigidly bound to an ion, the displacement of an ion induces a polarization which is equal to the charge of the ion times its displacement and Born effective charges are equal to the ion charge. A value of the Born charge different from the charge present on the displaced ion implies that displacement of that ion induces significant electronic currents in the nearby region. The phonon band structure of  $\alpha$ -PtO<sub>2</sub>, calculated by the methods explained in subsection 3.1.6, is reported in fig. 4.4, a summary of its vibrational properties is to be found in table 4.2.

It is quite rare that a transition metal oxide is held together by Van der Waals forces. Another example of an oxide with a layered structure held together by Van der Waals interactions is V<sub>2</sub>O<sub>5</sub> [72, 73]. The fact that the geometry of  $\alpha$ -PtO<sub>2</sub> is very similar to the sheet structure of graphite is also very interesting. This fact, together with the fact that 'needle-like' structures have been observed in  $\alpha$ -PtO<sub>2</sub> specimens [71], has motivated us to

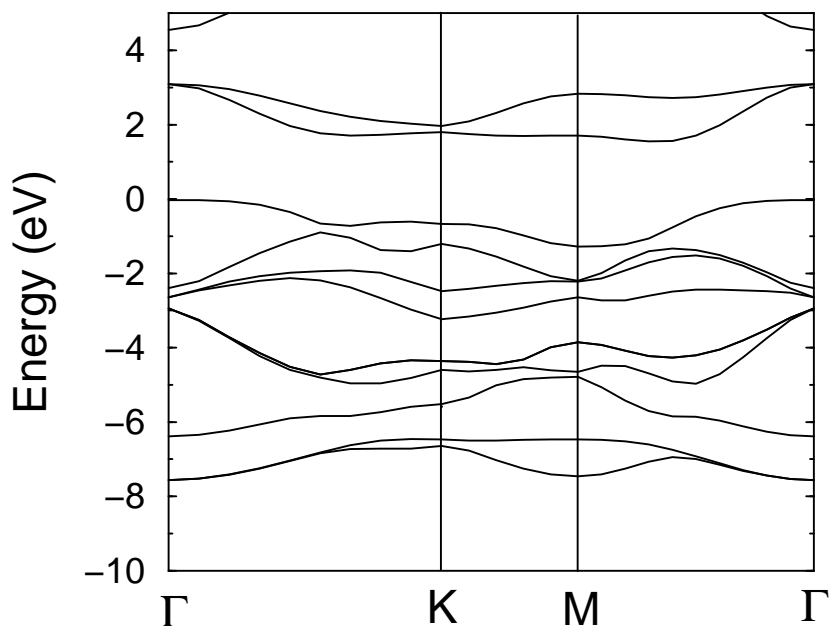


Figure 4.3: Electronic band structure of  $\alpha$ -PtO<sub>2</sub>; the zero of energy has been put to the top of the highest occupied band.

investigate the possibility of the existence of  $\alpha$ -PtO<sub>2</sub> nanotubes. Transition metal oxide nanotubes were fabricated in laboratory in the case of TiO<sub>2</sub> [74], as well as Pt nanoshell tubes [75], and they should display better catalytical activities due to the considerably enhanced surface-to-volume ratio compared to the bulk. In parallel it has been established through HRTEM that the needle-like structures seen in Ref. [71] consist of  $\alpha$ -PtO<sub>2</sub> sheet partly wound up around themselves, not of 'closed' nanotubes [76]. In  $\alpha$ -PtO<sub>2</sub> the lattice is triangular and not hexagonal as in graphite and there are two principal orientations for the nanotube axis: with the axis along a Pt-Pt nearest neighbour bond and with the axis in the middle between two nearest neighbour bonds. We have performed calculations only for the first kind of nanotubes, a model of which is shown in fig. 4.5. We have calculated total energy of small nanotubes without relaxation of atomic positions, to test whether formation of these structures could be energetically feasible. The size of the simulation cell has been chosen to keep a distance of  $\sim 8$  Å between two copies of the nanotube within periodic boundary conditions. In tab. 4.3 the results of total energy calculations are re-

Optical frequencies in $\Gamma$ ( $cm^{-1}$ )	480	498	498
	538	538	552
Frequencies in K	132	224	258
	458	469	499
	538	554	585
Frequencies in M	139	191	277
	405	492	522
	542	553	565
$\epsilon_{11}$ (electronic dielectric tensor)		2.05 (4.26)	
$\epsilon_{22}$		7.67 (11.15)	
$\epsilon_{33}$		7.67 (11.15)	
Born effective charges			
$Z_{Pt,11,22,33}$	0.54 (0.82)	4.02 (3.91)	4.02 (3.91)
$Z_{O,11,22,33}$	-0.27 (-0.41)	-2.01 (-1.95)	-2.01(-1.95)

Table 4.2: Phonon frequencies, dielectric tensor and Born effective charges of  $\alpha$ -PtO<sub>2</sub> (in parentheses LDA values). Non-diagonal terms of the electronic dielectric tensor and of the Born effective charges are not reported, as they are negligibly small.

ported together with their diameter, which is calculated as the distance between the two farthest oxygens. The diameter-dependence of the energy is roughly  $1/r^{2.3}$  as shown in fig. 4.6; the energy curve is slightly lower for nanotubes with a number of Pt atoms in the unit cell that is a multiple of 4. For comparison, in the case of carbon nanotubes, a  $1/r^2$ -dependence of the energy formation, taking a graphene sheet as reference, was established [77]. Nanotubes with  $\sim 1.2$  nm diameter have already a formation energy as low as 1.12 eV per formula unit, i.e. ca. 0.37 eV/atom. This value is comparable to the formation energy of a carbon nanotube with 7 Å diameter [77]. Since carbon nanotubes with this diameter have been observed, we conclude that formation of  $\alpha$ -PtO<sub>2</sub> nanotubes is at least energetically feasible.

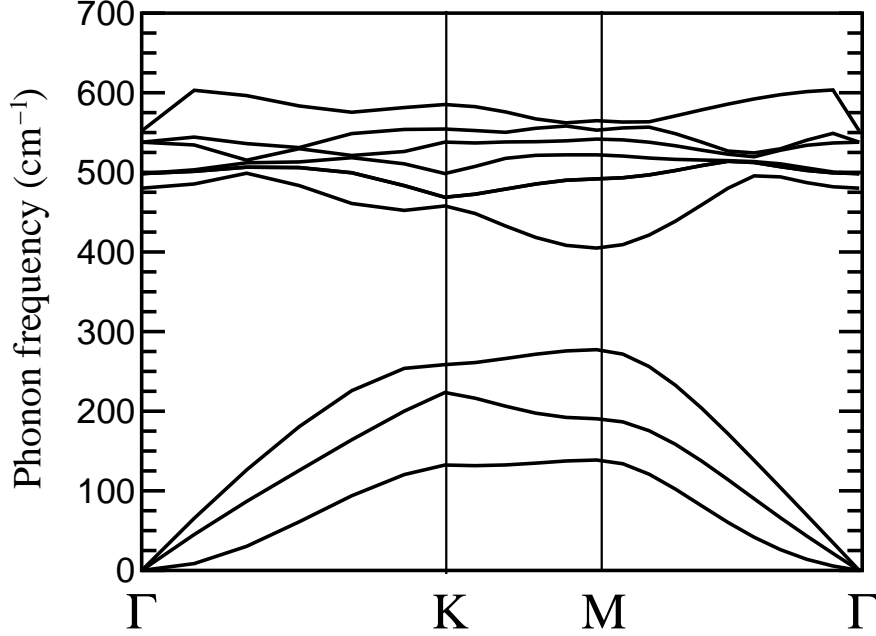


Figure 4.4: Phonon band structure of  $\alpha$ -PtO<sub>2</sub>.

#### 4.1.2 $\beta$ -PtO<sub>2</sub>

$\beta$ -PtO<sub>2</sub> crystallizes in an orthorhombic CaCl<sub>2</sub> structure, which is closely related to the rutile structure, differing from the latter only through a rotation of the oxygen pairs around the central Pt atom. This is quantified by the rotation angle or alternatively by the reduced coordinates  $x$  and  $y$  of the oxygen atoms. We calculate  $x = 0.26$  and  $y = 0.35$ , which corresponds to a rotation angle of 8.5° (to be compared with the experimental value of 7.7° [69], and with the value of 9.4° computed within DFT in Ref. [70] without optimization of  $b/a$  and  $c/a$ ). A transition from the CaCl<sub>2</sub> into the rutile structure has been predicted to occur at  $\sim 1240$  K [69]. We have calculated also the rutile structure and found a difference in energy between the two structures of 89 meV/formula unit (without zero-point energy) in favour of the CaCl<sub>2</sub> structure (Wu and Weber found a difference of  $\sim 200$  meV without optimization of  $b/a$  and  $c/a$  [70]); this small energy difference is compatible with the notion of a thermodynamic phase transition. Contrary to experimental evidence, but in agreement with previous DFT calculations [9],  $\alpha$ -PtO<sub>2</sub> is less stable than  $\beta$ -PtO<sub>2</sub> by about 10 meV/Pt

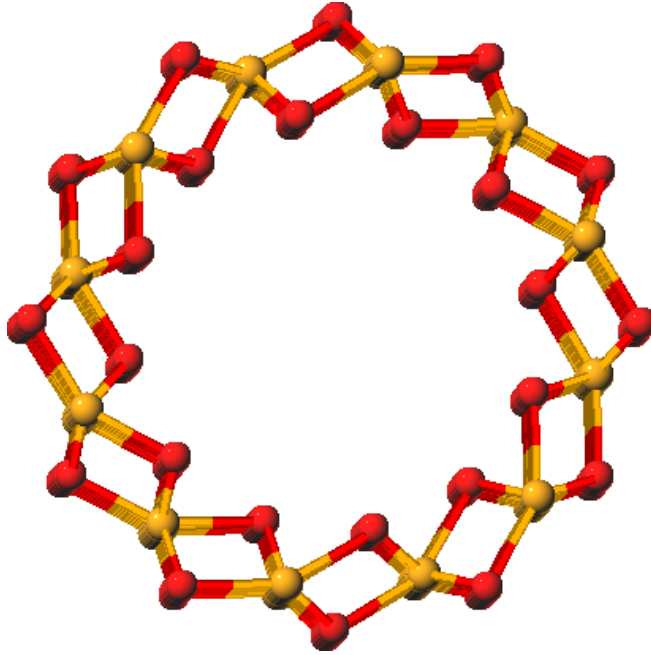


Figure 4.5: An  $\alpha$ -PtO<sub>2</sub> nanotube with 12 Pt atoms in unit cell ( $\sim 1.2$  nm diameter).

$N_{Pt}$	diameter (nm)	$\Delta E$ /formula unit (eV)	$N_{Pt}$	diameter (nm)	$\Delta E$ /formula unit (eV)
6	$\sim 0.7$	4.28	8	$\sim 0.8$	2.50
10	$\sim 1.0$	1.60	12	$\sim 1.2$	1.12
14	$\sim 1.4$	0.84			

Table 4.3: Formation energy per formula unit of  $\alpha$ -PtO<sub>2</sub> nanotubes in dependence of diameter.  $N_{Pt}$  is the number of Pt atoms in the unit cell, the reported diameter is the distance between the two farthest oxygens.



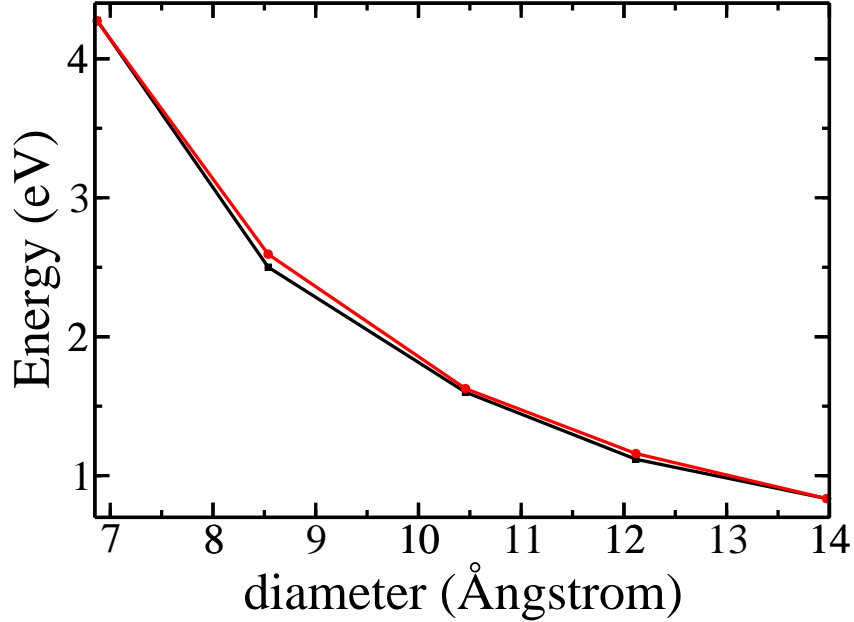


Figure 4.6: Energy of formation per formula unit of  $\alpha$ -PtO<sub>2</sub> nanotubes in dependence of diameter. Black line: DFT results; red line: function  $\frac{\alpha}{r^\beta}$ , with  $\beta=2.3$  and  $\alpha=359.698$  eV\*Å<sup>2.3</sup>, chosen to reproduce the DFT energy at the larger diameter considered.

atom. This is most probably due to the underestimation of the interlayer binding energy at the GGA level (37 meV/Pt atom). Indeed, considering the interlayer binding energy calculated at the LDA level ( $\sim 50$  meV/Pt atom) as a reasonable approximation for the real value (as is the case for graphite), then the  $\alpha$  isomorph becomes more stable, although only by about 2 meV/Pt atom. The calculated band gap is 0.43 eV, quite smaller than the 1.49 eV of  $\alpha$ -PtO<sub>2</sub> (see fig. 4.7 for the complete band structure). The Bader charges amount to +1.62 |e| for the Pt atoms and to -0.81 |e| for the O atoms. In comparison to  $\alpha$ -PtO<sub>2</sub> there is an additional charge transfer from the Pt atoms to the oxygens.

The calculated phonon frequencies at  $\Gamma$  (see fig. 4.8, tab. 4.4 and 4.5) are at least qualitatively in accordance with experimental Raman measurements [69], which found peaks in the Raman spectrum at  $\sim 205$  cm<sup>-1</sup>,  $\sim 340$  cm<sup>-1</sup> and  $\sim 610$  cm<sup>-1</sup> at 295 K, with a strong temperature dependence. The comparison of the vibrational properties of  $\alpha$ -PtO<sub>2</sub> and  $\beta$ -PtO<sub>2</sub> shows that the  $\beta$  isomorph displays higher eigenvalues of the electronic di-

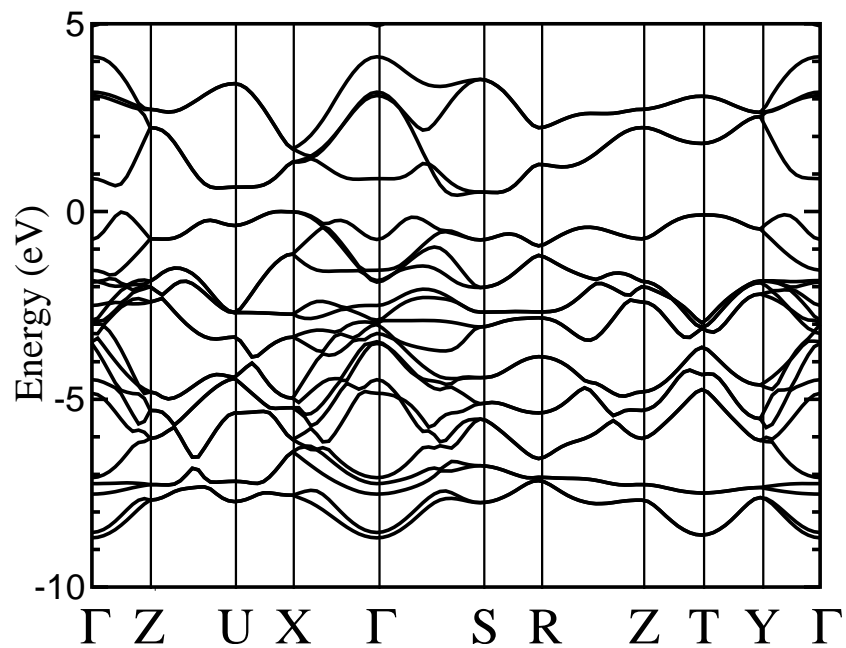


Figure 4.7: Electronic band structure of  $\beta$ -PtO<sub>2</sub>; the zero of energy has been put to the top of the highest occupied band.

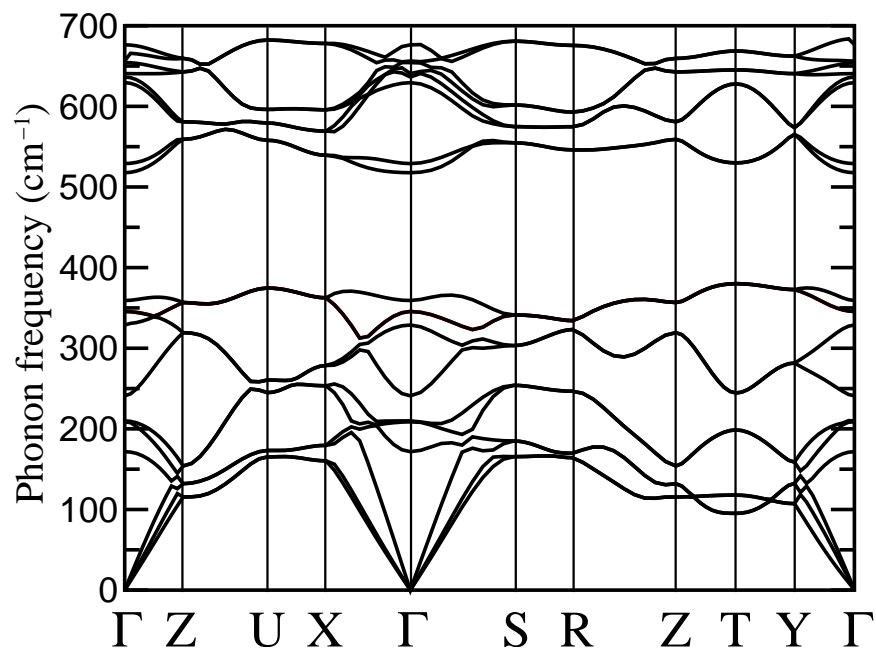


Figure 4.8: Phonon band structure of  $\beta$ -PtO<sub>2</sub>.

electric tensor and smaller eigenvalues of Born effective charge tensor. While the Born charge tensor for the displacement of a single ion in the primitive cell is not diagonal in the cartesian representation, the non-diagonal terms compensate so that the matrix associated with a displacement of the sublattice of *all* Pt atoms is again diagonal, so it is that associated with a displacement of the sublattice of *all* O atoms. This explains the fact that the high-frequency dielectric tensor is diagonal in the cartesian representation. The large anisotropy of the Born effective charge tensor is probably due to strong hybridization in this compound, which was studied more in detail by Wu and Weber [70].

In both PtO<sub>2</sub> oxides there is one eigenvalue of the Born effective charge tensor that is not only smaller than the nominal ion charge but also of the Bader charge. While in  $\alpha$ -PtO<sub>2</sub> this is connected with the direction perpendicular to the O-Pt-O trilayers, in  $\beta$  it is not clear to which feature of the crystal it is to be brought in connection with. Anyway in  $\beta$  this small eigenvalue exists only in presence of a displacement of only one oxygen atom of the four present in the primitive cell. If we consider the collective displacement of all the four oxygens in the cell (or of both platinum atoms), the non-diagonal terms cancel out while diagonal terms sum up, and one gets a diagonal matrix with eigenvalues -0.72, -0.98 and -1.35 per O atom. These values must be compared with the value of -0.81 of the Bader charge of the O ions, and show that the values in the x-y plane comply with the Bader charge, while in the z direction a larger value is found.

Despite the very different crystal structures and physical properties,  $\alpha$ -PtO<sub>2</sub> and  $\beta$ -PtO<sub>2</sub> have some structural similarity: in both solids the Pt atoms are in the center of an octahedron formed by six oxygens, and also the Pt-O distances are quite the same: 2.05 Å for  $\alpha$ -PtO<sub>2</sub>, 2.03 Å for  $\beta$ -PtO<sub>2</sub>. On the contrary the oxygens are very differently coordinated: off the Pt plane in  $\alpha$ , in the middle of a Pt 'triangle' in  $\beta$ .

Optical frequencies in $\Gamma$ ( $\text{cm}^{-1}$ )	172	209	210	241	329	346
	359	518	529	629	636	641
	654	656	676			
Frequencies in T	95	95	118	118	199	199
	245	245	380	380	530	530
	628	628	645	645	669	669
Frequencies in Y	107	107	132	132	159	159
	282	282	373	373	565	565
	574	574	641	641	662	662

Table 4.4: Phonon frequencies of  $\beta$ -PtO<sub>2</sub>.

### 4.1.3 Pt<sub>3</sub>O<sub>4</sub>

For Pt<sub>3</sub>O<sub>4</sub> there are two proposed crystal structures: body centered cubic (BCC) [26] or simple cubic (SC) [22]. In the case of the BCC structure, we have computed an optimized lattice constant is 5.49 Å, which is much smaller than the value of 6.226 Å originally proposed to explain the x-ray data. Moreover, the computed formation energy is 2.45 eV higher than the formation energy of the SC structure, for which the agreement between experimentally proposed and calculated lattice parameter (5.59 Å vs. 5.65 Å) is much better (table 4.1), so that we conclude that SC is the right structure for this phase. In this structure it is peculiar that all Pt atoms occupy equivalent position, which suggests that they all have the same fractional oxidation state 8/3. The hypothesis that all Pt atoms have the same oxidation state is confirmed by the calculation of the Bader charges, which amount to +1.13 |e| for each Pt and to -0.85 |e| for each O. The electronic structure of SC Pt<sub>3</sub>O<sub>4</sub> at the DFT-GGA level presents no band gap, i.e., the oxide appears to have metallic character. No other experimental or theoretical data are available, so we are not able to draw a definitive conclusion here. We have performed GGA+U calculations and even with values of U as high as 15 eV no electronic band gap has been observed, although most occupied bands have been considerably shifted downward in energy.

$\epsilon_{11}$ (electronic dielectric tensor)		19.56 (16.53)	
$\epsilon_{22}$		20.48 (17.18)	
$\epsilon_{33}$		24.75 (17.41)	
Born effective charges			
$Z_{Pt,11,12,13}$	1.45 (1.35)	$\pm 1.00$ ( $\pm 0.87$ )	-
$Z_{Pt,21,22,23}$	$\pm 1.51$ ( $\pm 1.12$ )	1.96 (1.72)	-
$Z_{Pt,31,32,33}$	-	-	2.70 (2.61)
$Z_{O,11,12,13}$	-0.72 (-0.68)	$\mp 0.67$ ( $\mp 0.72$ )	-
$Z_{O,21,22,23}$	$\mp 0.73$ ( $\mp 0.74$ )	-0.98 (-0.86)	-
$Z_{O,31,32,33}$	-	-	-1.35 (-1.31)
$Z_{//}^{Pt}, Z_{\perp}^{Pt}$ (eigenvalues of tensor)	0.45 (0.53)	2.96 (2.54)	2.70 (2.61)
$Z_{//}^O, Z_{\perp}^O$	-0.11 (-0.03)	-1.59 (-1.50)	-1.35 (-1.31)

Table 4.5: Dielectric tensor and Born effective charges of  $\beta$ -PtO<sub>2</sub> (in parentheses LDA values). For  $Z_{ij}$  the  $i$  represents the atom displacement, the  $j$  the component of the polarization. The  $Z_{//}$ 's and  $Z_{\perp}$ 's are the eigenvalues of the  $Z$  tensors. The non-diagonal terms of  $Z$  change sign for different atoms in the primitive cell, therefore they have a  $\pm$  symbol.

#### 4.1.4 PtO

The structure of PtO was described for the first time by Moore and Pauling [23]. Like PdO, which is the only stable palladium oxide, it has a tetragonal PtS crystal structure. The calculated band structure displays metallic character (fig. 4.10), even though PtO is believed to have a gap larger than 0.7 eV. The discrepancy has been thoroughly investigated and emerges in most existing GGA and local spin density approximation calculations [78, 79]; in one case [80] the appearance of the gap could be ascribed to the effect of the spherical augmentation of the wavefunction around the nuclei [79, 80]. On the contrary a hybrid functional with exact exchange gave a gap of 0.86 eV [78]. Notably, the absence of band gap could be corrected at the GGA+U level. A value of  $U$  of 9 eV gave a gap of 0.38 eV, an  $U$  of 15 eV a gap of 0.83 eV. The metal ions have a Bader charge of +0.86  $|e|$ , the

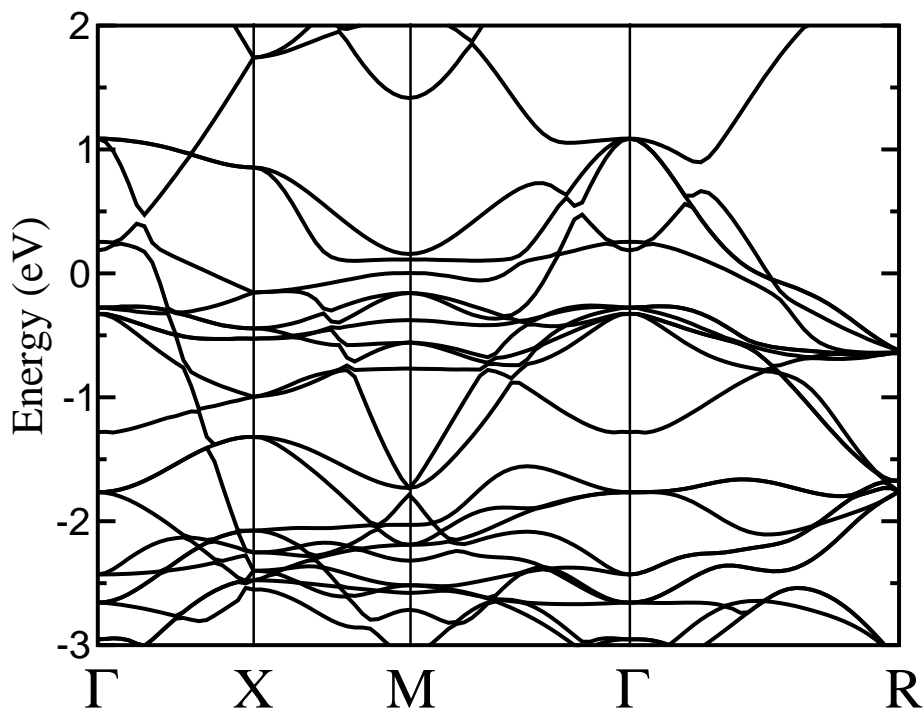


Figure 4.9: Electronic band structure of Pt<sub>3</sub>O<sub>4</sub>; the zero of energy has been put at the Fermi level.

oxygens  $-0.86 |e|$ .

PtO and Pt<sub>3</sub>O<sub>4</sub> are very similar both in stoichiometry and in atom coordinations. In both crystals the Pt atoms are surrounded by four square-planar oxygens, the main difference being that the oxygens in PtO are almost tetrahedrally coordinated to four Pt atoms, while in Pt<sub>3</sub>O<sub>4</sub> each O is surrounded by only three platinum atoms.

According to the coordinations of the Pt ions in the bulk, the four oxides may be classified in two categories: on one side the PtO<sub>2</sub> oxides, in which the Pt atoms are in the center of an octahedron built by six O atoms, on the other side Pt<sub>3</sub>O<sub>4</sub> and PtO, in which the Pt is in the center of a square of four O atoms, while other ions are further away. The oxides in each category then differentiate strongly from each other as far as the order of

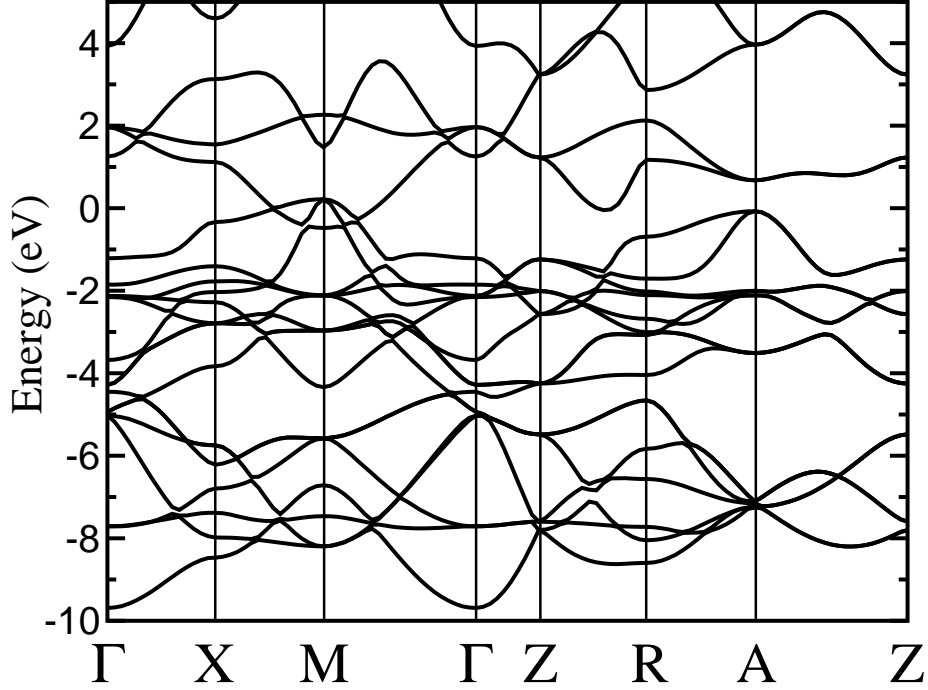


Figure 4.10: Electronic band structure of PtO; the zero of energy has been put at the Fermi level.

these basic structural elements (the  $\text{PtO}_6$  octahedrons and the  $\text{PtO}_4$  squares) in the bulk is concerned. This classification is reflected in the electronic properties: the  $\text{PtO}_2$  oxides have a clear gap even within GGA with plane waves, while the other two oxides do not display a gap in the simple GGA simulations with plane waves.  $\alpha$ - $\text{PtO}_2$  displays a well definite band gap of 1.49 eV,  $\beta$ - $\text{PtO}_2$  a gap of 0.43 eV. On the contrary  $\text{Pt}_3\text{O}_4$  and PtO have a metallic band structure within our approximations; while in the case of PtO this appears to be a well-known shortcoming of our simulation method (which in fact could be corrected at the GGA+U level), no other experimental or theoretical data exist for  $\text{Pt}_3\text{O}_4$ . Bader charges are roughly proportional to the nominal value of the oxidation state of the Pt ion: 1.53 |e| for  $\alpha$ - $\text{PtO}_2$ , 1.62 for  $\beta$ - $\text{PtO}_2$ , 1.13 for  $\text{Pt}_3\text{O}_4$  and 0.86 for PtO, so that the Bader charge of the O ions is roughly constant: 0.76 |e| for  $\alpha$ - $\text{PtO}_2$ , 0.81 |e| for  $\beta$ - $\text{PtO}_2$ , 0.85 |e| for  $\text{Pt}_3\text{O}_4$ , 0.86 |e| for PtO.

We have calculated the phonon band structure, the electronic dielectric tensor and the Born

effective charge (BEC) tensor of the two oxides with PtO<sub>2</sub> stoichiometry. Born effective charge tensors are very anisotropic for both  $\alpha$ -PtO<sub>2</sub> and  $\beta$ -PtO<sub>2</sub> and have one very small eigenvalue (0.54 for  $\alpha$ -PtO<sub>2</sub>, 0.45 for  $\beta$ -PtO<sub>2</sub>). This anisotropy is reflected in the electronic dielectric tensor. To our knowledge very few crystals have been found to have unusually small eigenvalues of the BEC tensor, one example being  $\alpha$ -quartz [81], while much more attention has been devoted to large anomalous BEC's in oxides on the verge of phase transitions [47, 82].

#### 4.1.5 Ab-initio thermodynamics of bulk oxides

In table 4.6 the enthalpies of formation at T=0 K, p=0 atm are reported, together with some calculated or measured values from the literature.

Fig. 4.11 shows the phase diagram for the Pt-O system for low-pressure oxide phases. By taking into account the energy associated with the Van der Waals interaction between trilayers in  $\alpha$ -PtO<sub>2</sub> as estimated by LDA we find that  $\alpha$ -PtO<sub>2</sub> is slightly favoured over  $\beta$ -PtO<sub>2</sub> at T=0 K, p=0 atm; this is in agreement with the experimental finding that  $\beta$ -PtO<sub>2</sub> is stable in bulk form only above 200 atm oxygen pressure [22].

Important points are that 1)  $\alpha$ -PtO<sub>2</sub> is the stable phase at low temperatures, metallic Pt is stable at high temperature, and in between there is a region of stability of Pt<sub>3</sub>O<sub>4</sub>. This region is ca. 100 K wide and at 1 atm oxygen pressure it extends from 870 K to 974 K. Transition temperatures move to lower values at lower O<sub>2</sub> pressures, without qualitative changes. The only data available at atmospheric pressures are those of Punnoose [24], who found transitions to take place at 910 K and 1070 K for supported clusters, and lie therefore in the same range as our results. These discrepancies are acceptable within our method, also taking into account that Punnoose didn't work with bulk phases but with supported clusters. Saenger and co-workers [87] investigated the time-dependent behaviour of a Pt(O) film, and found the formation of a short-lived crystalline Pt<sub>3</sub>O<sub>4</sub> at 920 K in oxygen during the decomposition of an amorphous film of PtO<sub>x</sub> with x  $\sim$ 1.4. Zakharchenko [88] found that, while Pt<sub>3</sub>O<sub>4</sub> is easily reduced to Pt in an ammonia-rich atmosphere at temperatures



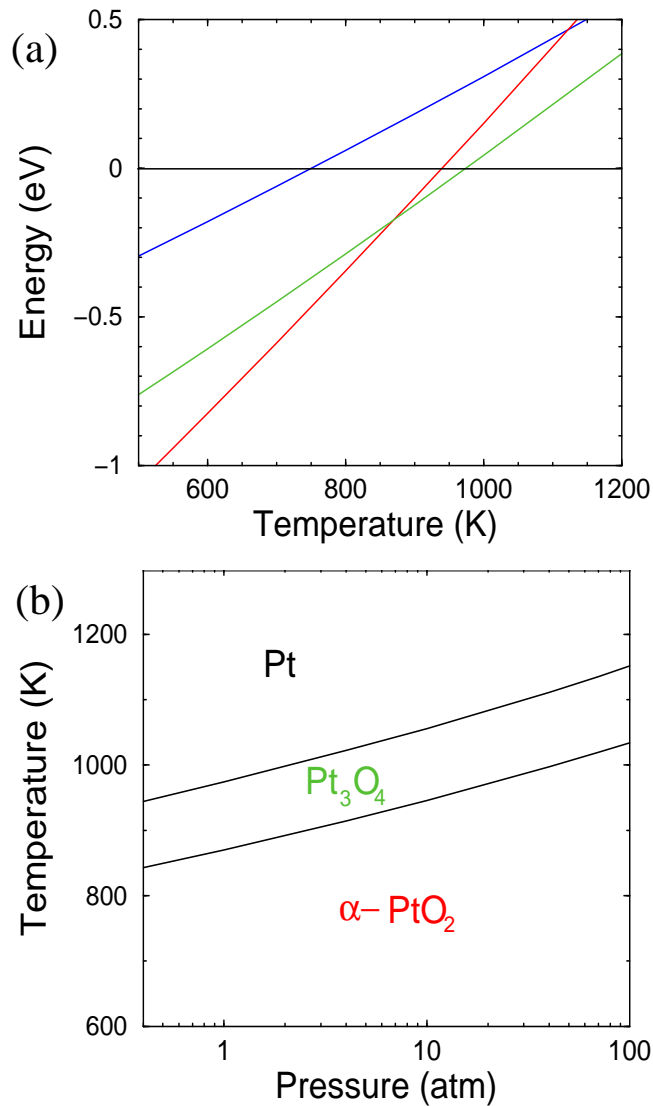


Figure 4.11: Bulk platinum oxides: (a) Gibbs' free energies of formation of  $\alpha$ -PtO<sub>2</sub> (red), Pt<sub>3</sub>O<sub>4</sub> (green), PtO (blue) and metallic platinum (horizontal black line, for reference) at 1 atm oxygen pressure; (b) Phase diagram for bulk platinum oxides in dependence of oxygen pressure and temperature

above 963 K, the reduction doesn't take place after 3 hours at lower temperatures under the same conditions.

2) Pt<sub>3</sub>O<sub>4</sub> has a simple cubic structure, since the other proposed structure has not only a

Compound	$\Delta H_f(0, 0)$ ( $E_{cut}=50$ Ry)	$\Delta H_f(0, 0)$ ( $E_{cut}=70$ Ry)	exp. data	other DFT [9]
$\alpha$ -PtO <sub>2</sub>	-2.05	-2.11	-190 kJ/(mol O <sub>2</sub> ) [25] (-222 [83]) (-167±42 [84])	-0.62 eV/O atom
$\beta$ -PtO <sub>2</sub>	-2.06	-2.13		-0.64 eV/O atom
Pt <sub>3</sub> O <sub>4</sub>	-1.42	-1.51	-184 kJ/(mol O <sub>2</sub> ) [25] (-163 [85])	
BCC-Pt <sub>3</sub> O <sub>4</sub>	+1.03			
PtO	-0.76	-0.89	-180 kJ/(mol O <sub>2</sub> ) [25] (-142 [86])	-0.41 eV/O atom

Table 4.6: Calculated Gibbs' free energy of formation of Pt oxides at  $T = 0$  K,  $p = 0$  atm (in eV/Pt atom) and some experimental and DFT data. For each oxide, the first experimental data is measured at 770 K.

very different lattice constant from the one proposed in literature, but it has also a much higher Gibbs' free energy than all other oxide phases.

3) PtO exists only as metastable phase. This is a striking difference from isoelectronic palladium, for which PdO, which is isostructural to PtO, represents the only stable oxide [89].

The diagram has been calculated without taking into account phonon contributions. To estimate the error, we have calculated phonon contributions for  $\alpha$ -PtO<sub>2</sub> and Pt, and found that the  $\alpha$ -PtO<sub>2</sub>-Pt equilibrium point at 0.4 atm is shifted from 936 K to 966 K by adding these contributions. Since such a shift is smaller than the expected errors for this method [6], neglecting the phonon contributions is not expected to affect our main conclusions.

## 4.2 Surfaces

Since we are interested in the catalytic activity of oxidized platinum, it is important to determine the thermodynamic stability of exposed surfaces. We have therefore calculated the surface free energy (see eq. 3.19) of a number of low-index surfaces of the metallic and oxide phases using symmetric slab models. Results for regular surfaces of platinum and Pt oxides are reported in table 4.7, structures of selected oxide surfaces are shown in fig. 4.12. In the case of metallic platinum we consider here the two lowest-energy surfaces, namely (111) and (100), which correspond to the common termination of metallic nanoparticles [11]. Pt(111) is the surface with the lowest surface energy, as it is typical for FCC

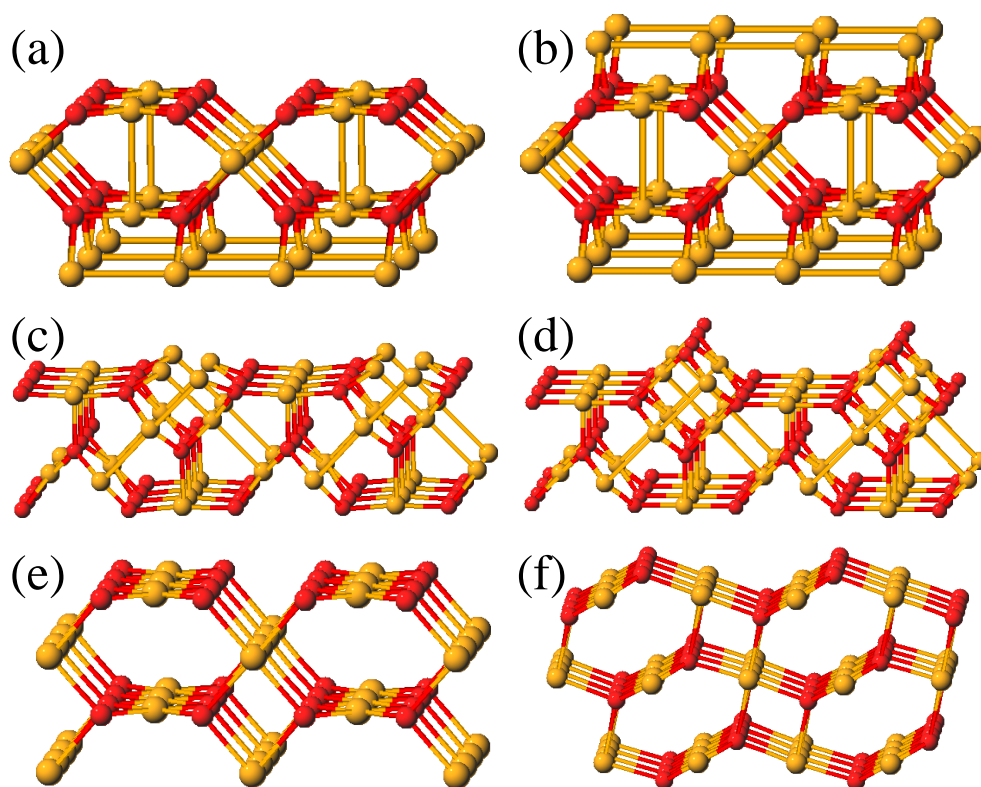


Figure 4.12: Regular surfaces of platinum oxides: (a)  $\text{Pt}_3\text{O}_4(100)$ -O-terminated; (b)  $\text{Pt}_3\text{O}_4(100)$  -Pt-terminated; (c)  $\text{Pt}_3\text{O}_4(110)$ -Pt-terminated; (d)  $\text{Pt}_3\text{O}_4(110)$ -O-terminated; (e)  $\text{PtO}(100)$ -O-terminated; (f)  $\text{PtO}(101)$ .

Surface	Surface free energy (meV/Å <sup>2</sup> )	Surface	Surface free energy (meV/Å <sup>2</sup> )
Pt(111)	103	Pt <sub>3</sub> O <sub>4</sub> (100)-O	27
Pt(100)	131	Pt <sub>3</sub> O <sub>4</sub> (100)-Pt	128
$\alpha$ -PtO <sub>2</sub> (0001)	2	Pt <sub>3</sub> O <sub>4</sub> (110)-O	77
		Pt <sub>3</sub> O <sub>4</sub> (110)-Pt	187
PtO(101)	56	PtO(100)	-31

Table 4.7: Regular surfaces of platinum oxides; the Pt<sub>3</sub>O<sub>4</sub> and PtO surfaces are those sketched in fig. 4.12

metals. Pt(100) is known to display a quasi-hexagonal reconstruction under ultra-high vacuum (UHV) conditions; this Pt(100)-hex structure has a  $(5 \times 20)$  periodicity and undergoes a rotation by  $0.7^\circ$  at 110 K to become a Pt(100)-hex- $\mathbf{R}0.7^\circ$  [90]. It was shown that the reconstruction is lifted already at very low CO [91] and H<sub>2</sub> [92] pressures, therefore unreconstructed Pt(100) has been considered, since we are interested in applications in natural atmosphere.

As pointed out in the previous section,  $\alpha$ -PtO<sub>2</sub> is held together only by weak Van der Waals forces in the (0001) direction, and therefore we expect only the (0001) surface to be relevant. On this surface Pt atoms are ordered on a triangular lattice like on a Pt(111) surface, but with a larger Pt-Pt distance of 3.14 Å (see table 4.1) against 2.82 Å on Pt(111) (experimentally 2.77 Å).

For Pt<sub>3</sub>O<sub>4</sub> we have considered the (100) and (110) surfaces; the (100) in its oxygen-rich termination displays rows of platinum atoms, each atom being at the center of a square of oxygen atoms (see fig. 4.12). Only every second O-square has a Pt at the center, so that each oxygen is bound only to two Pt atoms. The Pt-Pt distances in a row and between rows are 5.65 Å, while on Pt(100) Pt-Pt distances are 2.82 Å, which is the half of 5.65 with an error of less than 1%, so that a coherent interface Pt/Pt<sub>3</sub>O<sub>4</sub> can form. The geometry of Pt<sub>3</sub>O<sub>4</sub>(100) is very similar to that of PtO(100), with the important difference that on

PtO(100) every O-square has a Pt atom in the center; the platinum density on the surface is higher and each oxygen is bound to three Pt atoms. As far as PtO is concerned, even if this is a metastable phase, we cannot exclude a priori the formation of thin PtO films as result of platinum oxidation processes. We have thus taken into account the PtO(100) and the PtO(101) surfaces (see fig. 4.12). In the next subsection we show that, while bulk PtO is a metastable phase, PtO-like monolayers may form on Pt(100).

Common features of these oxide surfaces are that the surface free energies are much smaller than those of metallic surfaces and that surfaces prefer oxygen-rich terminations at low temperatures.

### 4.3 Thin films

While bulk oxide phases are thermodynamically stable at low temperatures, it is common knowledge that platinum surfaces do not undergo spontaneous oxidation. The formation of bulk oxide is therefore expected to be kinetically hindered at room temperature. However, the formation of thin films of superficial oxide, which protects the bulk metal from further oxidation, cannot be excluded. Under conditions where thin oxide films are either thermodynamically or kinetically stable with respect to the bulk oxide phase, the structure and stoichiometry of such films do not necessarily correspond to bulk phases [4, 21]. On Pt(111) oscillatory kinetics of CO oxidation in 0.01 mbar oxygen pressure at  $\sim 400$  K was attributed to an oxidation-reduction cycle of the surface [93]. Formation of thin oxide films has been established on Pt(100) at submillibar oxygen pressures but not characterized with atomic resolution [94]. Formation of strongly bound oxygen has been shown to occur on Pt(100) in an oxygen pressure of  $9 \times 10^{-2}$  mbar at 473 K and to lead to catalyst deactivation [95]. The thermal desorption spectra have two maxima at 1020 K and 1160 K, and this high thermal stability is brought by McMillan and co-workers [95] as support for their opinion that this oxygen species forms a surface oxide, although composition and structure have not been further characterized. A thin oxide film was better characterized on Pt(110) [9]. Also on the Pd(100), isostructural to Pt(100), thin oxide film formation was observed

and its structure established [4]. On this surface a  $\sqrt{5} \times \sqrt{5}$   $\mathbf{R}27^\circ$  oxide monolayer was observed at ambient pressures at temperatures below 675 K, while formation of a bulk oxide (with 40 Ångstrom thickness) formed only at higher temperature, although ab-initio thermodynamics calculations suggest this structure to be thermodynamically more stable. Therefore we have to take into account the possibility that formation of monolayer-thin oxide films at the surface may occur, while the inner platinum remains reduced.

We have investigated a variety of oxide structures on the Pt(111) and Pt(100) surfaces up to a coverage of 1 ML of oxygen, with particular attention paid to possible coherent interfaces, and considering structures proposed in the existing literature for the oxidation of palladium [4] and platinum [10] surfaces. These give information about initial steps of oxidation of the surface and represent metastable states that exist in cases where further oxidation is kinetically hindered. The relevant monolayers are shown in fig. 4.13. The surface systems have been modeled with a slab with 5 Pt layers, either symmetric or with the oxygens only on one side and on the other side a clean metallic surface, to minimize computational effort on the bigger systems. In the latter case, surface free energies have been calculated (see eq. 3.19) assuming that the surface energy of the clean side is that of the clean metallic surface, which causes an error of less than 10 meV/Å<sup>2</sup>.

### 4.3.1 Pt(111)

We start our investigation with the adsorption of oxygen atoms in FCC-hollow sites of the (111) surface. Using a  $(2 \times 2)$  surface unit cell, the oxygen coverage can be varied from 0.25 to 1.0 ML. The average binding energy of an oxygen atom chemisorbed on the surface decreases significantly with increasing oxygen coverage, from 1.62 eV/O atom at 0.25 ML through 1.01 eV/O atom at 0.75 ML to reach a value of 0.59 eV/O atom at 1.0 ML, in agreement with experimental measurements [96]. Indeed, from thermal desorption spectra a reduction of the average binding energy of O on Pt(111) from 188 kJ/mol ( $\sim 1.95$  eV/O atom) at 0.25 ML to 109 kJ/mol ( $\sim 1.13$  eV/O atom) at 0.76 ML oxygen coverage was estimated. Significantly, at 0.75 ML coverage further adsorption is endothermic by 0.67

eV/O atom, so that the 0.75 ML O is the energetically favourable chemisorbed state, in excellent agreement with the experimental finding that at higher coverage oxide formation begins [96]. As can be seen in figure 4.15(a), at 1 atm of partial oxygen pressure a complete monolayer of adsorbed oxygen is not stable in any temperature interval. Instead, 0.75 ML is the stable adsorption coverage up to about 500 K, where the interval of stability of 0.5 ML begins, again in agreement with thermal desorption spectra that display desorption peaks at 560 K and 650 K for the chemisorbed oxygen [96]. Increasing the temperature is expected to lead to further oxygen desorption (0.25 ML is the stable coverage at T higher than about 850 K), until the bare metallic surface becomes the most stable phase at about 1400 K. We can thus expect that coverages higher than 0.75 ML can only be obtained by overcoming the enthalpy barrier towards insertion of oxygen atoms under the surface, with formation of a thin oxide layer. In literature, possible formation of thin films of  $\alpha$ -PtO<sub>2</sub> on Pt(111) is reported [10]. On  $\alpha$ -PtO<sub>2</sub>(0001) Pt atoms occupy a triangular lattice as on Pt(111), with a difference in Pt-Pt distance: 2.82 Å on Pt(111), 3.14 Å on  $\alpha$ -PtO<sub>2</sub>(0001). We have considered an  $\alpha$ -PtO<sub>2</sub> monolayer in two situations: a (1 × 1) structure, where there is a one-to-one correspondence between Pt atoms in the oxide layer and Pt atoms in outer metallic layer, obtained through compression of the oxide, and a (2 × 2) structure with an  $\alpha$ -PtO<sub>2</sub> monolayer, where the misfit strain in the oxide layer is reduced to only about 3%. Such a structure can be the outcome of the oxidation of the first layer of the metallic surface, when the resulting oxide layer relaxes over the edge of the surface. This structure proves to be the most stable at low temperatures. The compressed (1 × 1) oxide layer lies much higher in energy. At higher temperatures there is a transition to an unreconstructed Pt(111) with adsorbed oxygen in FCC-hollow positions with a coverage of 0.25 ML (see fig. 4.15(a)).

### 4.3.2 Pt(100)

On this surface the platinum atoms are ordered on a square lattice. To create such a surface from a bulk Pt specimen, four bonds must be broken for each surface platinum,

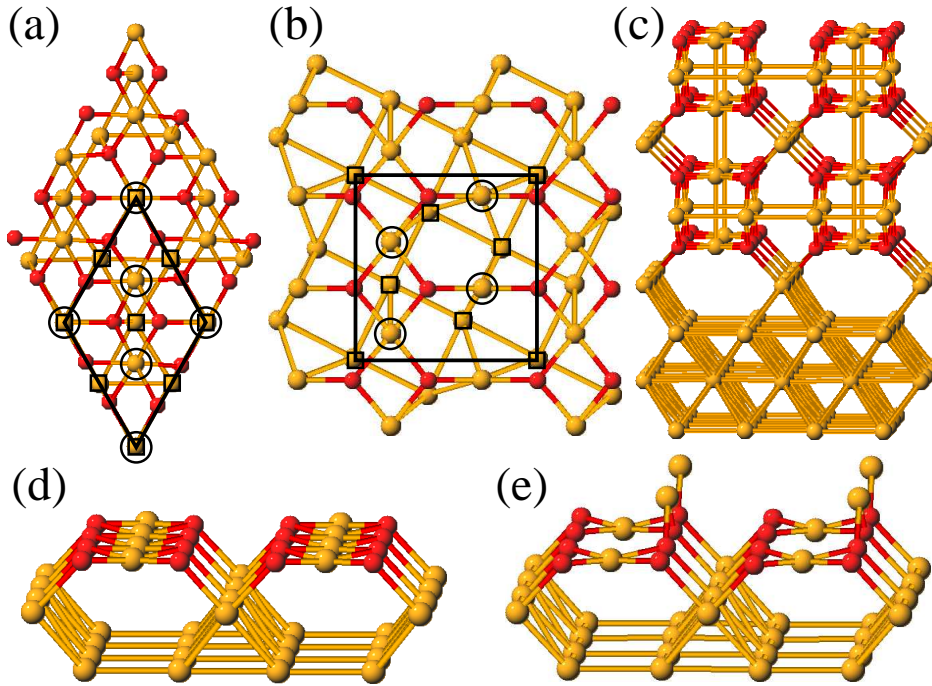


Figure 4.13: Oxide monolayers on Pt surfaces: (a)  $(2 \times 2)$   $\alpha$ -PtO<sub>2</sub> on Pt(111); the line delimitates the elementary surface cell, the squares indicate the positions of the Pt atoms in the topmost metallic layer, the circles indicate the positions of the Pt atoms in the oxide monolayer; (b)  $\sqrt{5} \times \sqrt{5} \mathbf{R} 27^\circ$  oxide monolayer on Pt(100); the symbols have the same meaning as in (a); (c) three Pt<sub>3</sub>O<sub>4</sub> monolayers on Pt(100); (d) PtO-like monolayer on Pt(100); (e) Pt<sub>3</sub>O<sub>4</sub>-like monolayer on Pt(100); (e) is obtainable from (d) by lifting every second Pt atom above the surface.

versus only three for Pt(111), therefore the surface energy of this surface is higher. On the unreconstructed surface oxygen atoms adsorb preferentially on bridge positions [97]. We have studied the relative stabilities of 0.5 ML and 1.0 ML of adsorbed oxygen, and find that the two curves cross at a temperature of about 772 K.

Pt(100) is isostructural to Pd(100), on which formation of a thin  $\sqrt{5} \times \sqrt{5} \mathbf{R} 27^\circ$  surface oxide has been observed [4]. This structure consists of a single PdO(101) layer adsorbed on Pd(100). The corresponding structure on Pt(100) relaxes substantially: while in the original PtO(101) layer oxygens are either lower or higher than the neighbouring Pt atoms,



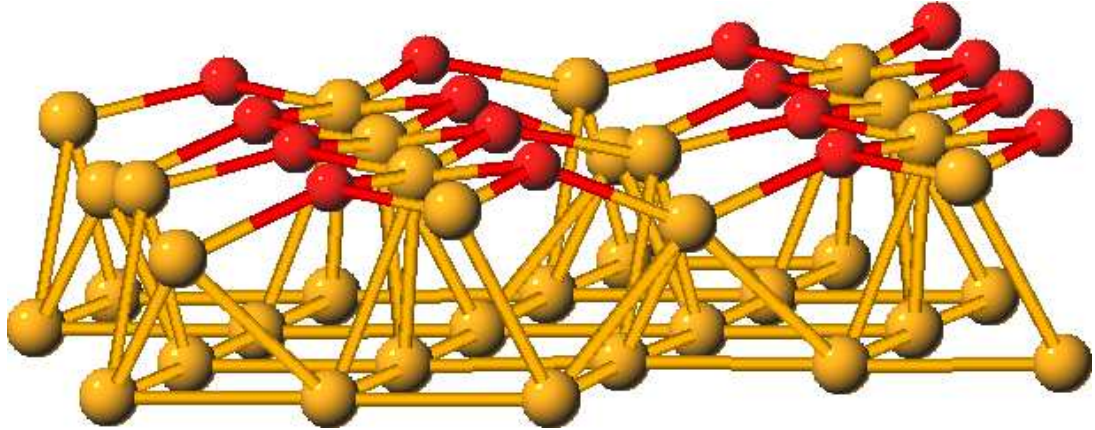


Figure 4.14: The relaxed  $\sqrt{5}X\sqrt{5}R27^\circ$  structure on Pt(100).

after relaxation the O atoms and the Pt atoms lie all almost on the same level. The relaxed structure is shown in fig. 4.13(b) and fig. 4.14. As already pointed out in the previous section, the disposition of Pt atoms on PtO(100) and on Pt<sub>3</sub>O<sub>4</sub>(100) is very similar to that on Pt(100), so that PtO-like and Pt<sub>3</sub>O<sub>4</sub>-like oxide monolayers could grow coherently on Pt(100). The two monolayers differ in the position of outer Pt atoms: in the PtO-like structure these Pt atoms occupy all the centers of the oxygen squares, while in the Pt<sub>3</sub>O<sub>4</sub>-like structure half of the oxygens are lifted to bridge positions between two oxygens (see fig. 4.13(d)-(e)).

An important difference is that, while Pt<sub>3</sub>O<sub>4</sub> can grow epitaxially on Pt(100) (less than 1% lattice mismatch), the PtO-like monolayer is compressed by 9% in the direction of the Pt rows and strained by 4% in the other with respect to the bulk PtO(100) surface. In fig. 4.15 the surface free energies at 1 atm oxygen partial pressure are reported. The PtO-like monolayer is the stable phase at low temperature, while the  $\sqrt{5}X\sqrt{5}R27^\circ$  structure is metastable. Formation of a Pt<sub>3</sub>O<sub>4</sub>-like monolayer is energetically unfavourable. At around 1000 K there is a transition to an unreconstructed surface with 0.5 ML chemisorbed oxygen. The PtO-like monolayer lies lower in energy than the Pt<sub>3</sub>O<sub>4</sub>-like monolayer, but, while the former is compressed, the latter grows epitaxially on Pt(100). As a consequence, as the oxide film becomes thicker, the Pt<sub>3</sub>O<sub>4</sub>-like becomes energetically more favourable. The

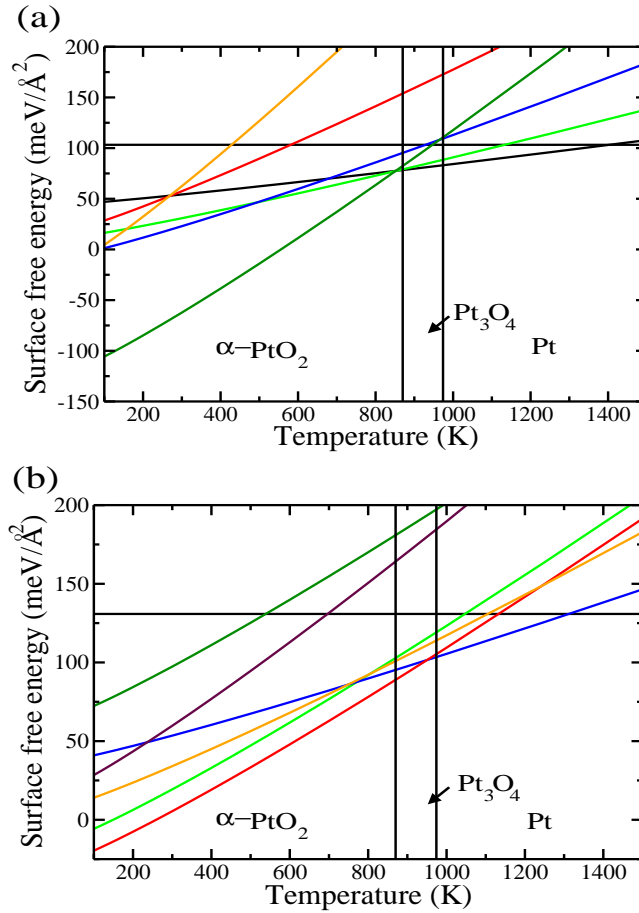


Figure 4.15: Surface free energies of oxidic systems on Pt surfaces at 1 atm oxygen pressure (the vertical black lines delimitate the stability regions of indicated bulk oxides): (a) on Pt(111): (2X2)  $\alpha$ -PtO<sub>2</sub> monolayer (ML) (see fig. 4.13(a)) (dark green); (1X1)  $\alpha$ -PtO<sub>2</sub> ML (orange); 1 ML adsorbed oxygen (1 ML O) (red); 0.75 ML O (blue); 0.5 ML O (light green); 0.25 ML O (black, growing); the horizontal black line is the surface energy of clean Pt(111). (b) on Pt(100): PtO-like ML (see fig. 4.13(d)) (red); PtO-like ML with adsorbed oxygen (brown); 1 ML O (light green); 0.5 ML O (blue);  $\sqrt{5} \times \sqrt{5} \text{R}27^\circ$  (orange); Pt<sub>3</sub>O<sub>4</sub>-like ML (see fig. 4.13(e)) (dark green); the horizontal black line is the surface energy of clean Pt(100).

3 ML thick Pt<sub>3</sub>O<sub>4</sub>-like structure is more stable than the 3 ML PtO-like structure up to  $\sim 1250$  K at an oxygen pressure of 1 atm.

## 4.4 Clusters

Addressing the question of  $\text{Pt}_3\text{O}_4$  formation, we have to consider that in technologically relevant applications in catalysis platinum is present in the form of clusters. Since these clusters are of primary importance in heterogeneous catalysis, we are interested in understanding how stability of oxide phases is modified by the finite size of these structures. With DFT one can calculate systems with at most a few dozens transition metal atoms, and this makes it possible to simulate models of bulk systems and surfaces also thank to the adoption of periodic boundary conditions. On the contrary nanometer-sized clusters are too large to be directly simulated, and their energy has to be calculated by a different approach. The total energy of a cluster can be expressed in terms of bulk energy plus energy of the defects present in the cluster, such as surfaces, edges, vertices:

$$E = e^{bulk} * V + \sum_i e_i^{surf} * S_i + \sum_j e_j^{edge} * L_j + \sum_m e_m^{vertex} * N_m \quad (4.1)$$

where the  $e$ 's are energy densities. Giving the number of Pt atoms in the cluster fixes the volume and therefore the volume contribution to the total energy, still the other contributions must be minimized. If the cluster is large enough, contributions of 0-D and 1-D defects can be overlooked and minimizing total energy amounts to minimizing surface energy at fixed volume. The cluster that minimizes surface energy at fixed volume is the one obtained by Wulff's construction (WC) [98]. The WC works in this way: fixed one point in space (the center of the cluster), segments are built from this point in the relevant crystallographic directions. These segments have a length proportional to the surface energy of the surface with that orientation. At the extremity of the segment a surface perpendicular to the segment is built. The internal envelope of all these surfaces is the external surface of the equilibrium cluster. It is clear that crystallographic surfaces with a large surface energy will have a long segment and therefore fall outside of the envelope. Only low-energy surfaces will be present on the surface of the cluster. Once determined the cluster form, the difference in Gibbs' free energy between a cluster of  $\text{PtO}_x$  and the metallic cluster with

the same number of Pt atoms can be calculated from bulk and surface contributions:

$$\Delta G_{cluster} = N_{Pt}(g_{PtO_x}^{bulk} - g_{Pt}^{bulk} - \frac{x}{2}g_{O_2}^{gas}) + (\sum_i A_i \gamma_i^{PtO_x} - \sum_j A_j \gamma_j^{Pt}) \quad (4.2)$$

where the  $g$ 's are Gibbs' free energies per formula unit, the  $A$ 's surface areas, the  $\gamma$ 's are surface free energies, and the sums over  $i$  and  $j$  run over  $PtO_x$  surfaces and Pt surfaces respectively.

The Wulff's construction relies on the possibility to overlook the energy of edges and vertices. For this to be justified, the cluster must be large enough. Theoretical works exist that give an estimation on how small metallic clusters must be to deviate from the form of the Wulff's polyhedra. For example in the case of Cu clusters, simulations with empirical potentials showed that for clusters with more than  $\sim 2500$  atoms the Wulff's polyhedron (a truncated octahedron in this case) has indeed the lowest total energy per atom, while smaller clusters prefer a icosahedral form with 20 triangular FCC (111) faces [99, 100]. This number of atoms corresponds to diameter of 3.8 nm [100].

For Pt we have taken into account the (100) and (111) surfaces. We have obtained clusters in form of irregular truncated octahedrons, with the irregular hexagons with (111) orientation sharing the short edges with (100) squares. The relation between long ( $b$ ) and short ( $a$ ) edges is  $b/a = 1.58$ . 14% of the surface is Pt(100), the rest is Pt(111). Since cluster diameter in real systems is often estimated from dispersion (defined as number of Pt atoms present on cluster surface divided by total Pt atom number [12]) from CO adsorption experiments, we report also calculation of dispersion as function of diameter for our model to help better estimate cluster diameter from experiment. The calculated dispersion (see fig. 4.16) is higher than the one estimated for supported clusters [101, 102], which is in accordance with the fact that on supported clusters part of the external surface is in contact with the support.

For  $Pt_3O_4$  we have considered the (100) and (110) surfaces. It turns out that the (110) is so high in energy (see tab. 4.7) that Wulff's clusters of  $Pt_3O_4$  are cubes with only (100) surfaces. For (110) to be present in the cluster, the surface free energies should have satisfied the relation  $\gamma_{(110)} < \gamma_{(100)}\sqrt{2}$ . Surface free energy of  $\alpha$ - $PtO_2(0001)$  is only 2 meV/ $\text{\AA}^2$ ,

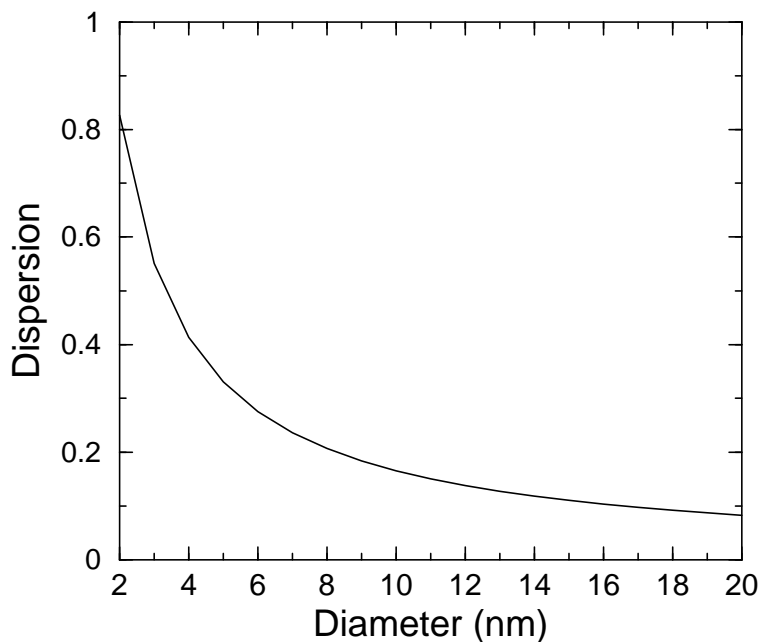


Figure 4.16: Dispersion of Pt clusters as function of diameter. The distance between two opposite (100) faces has been taken as diameter.

so that an  $\alpha$ -PtO<sub>2</sub> cluster is expected to be composed by an isolated O-Pt-O trilayer.

We have considered a metallic cluster and compared its Gibbs' free energy to that of Pt<sub>3</sub>O<sub>4</sub> and  $\alpha$ -PtO<sub>2</sub> clusters with the same number of Pt atoms. For small clusters the stability region of Pt<sub>3</sub>O<sub>4</sub> moves to higher temperatures and shrinks with respect to fig. 4.11, stability region of  $\alpha$ -PtO<sub>2</sub> expands to higher temperatures, as shown in fig. 4.17. A remarkable feature of this phase diagram is that, for small clusters, the diameter dependence of the transition temperatures is so strong that, if the cluster size distribution is broad enough, there exists no temperature at which all clusters can be in the Pt<sub>3</sub>O<sub>4</sub> phase in thermodynamic equilibrium. This is of particular importance in view of the finding, which we report in the next chapter, that Pt<sub>3</sub>O<sub>4</sub> should be a very good oxidation catalyst while  $\alpha$ -PtO<sub>2</sub> should be inactive for these reactions. If the cluster size distribution is broad, no matter what temperature is chosen for a heat treatment, one will probably get considerable amounts of  $\alpha$ -PtO<sub>2</sub> during the heat treatment.

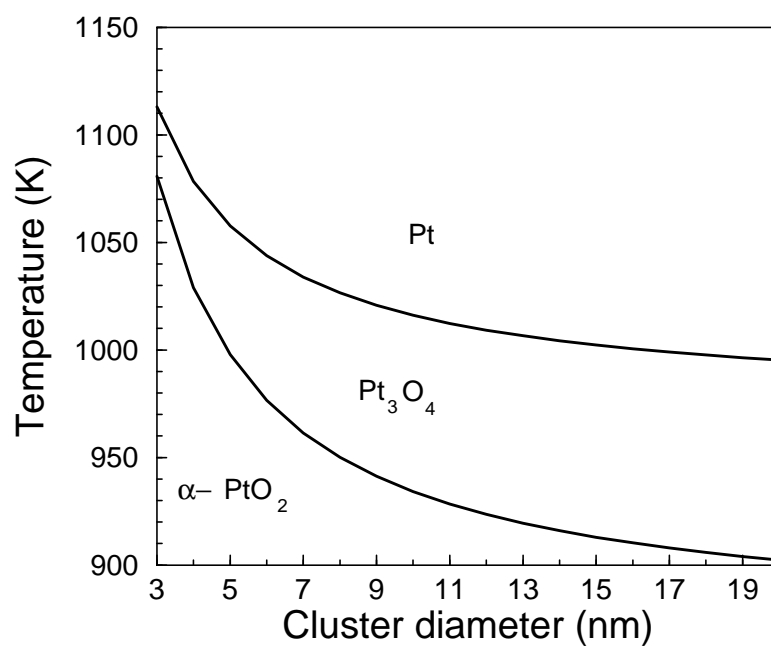


Figure 4.17: Phase transition temperatures as function of Pt cluster diameter. The distance between two opposite (100) faces in the metallic cluster has been taken as diameter.

# Chapter 5

## Catalysis

We have investigated how the presence of an oxide phase on the surface of the platinum catalyst affects the interaction of the catalyst with two carbon compounds: methane and carbon monoxide.

### 5.1 Dissociative adsorption of methane

Methane combustion is an important step in energy production for both private and industrial applications for its high energy content: the enthalpy of combustion at 298,15 K amounts to 890.8 kJ/mol (9.23 eV/molecule) [103] for the complete reaction to CO<sub>2</sub> and water. The total oxidation process can be very complicated, with competition of more reaction paths and with appearance of byproducts like formaldehyde, methanol, carbon monoxide. Clarification of all steps that, starting from a methane molecule, lead to CO<sub>2</sub> release in the gas phase is a challenging task, and the relative importance of different reaction paths is heavily dependent on reaction conditions [104]. On the other side we are not interested in predicting absolute values of activities and conversion rates on the different catalyst surfaces. Our aim is rather to establish which oxide phase has the highest activity, leaving to the experiments the task to determine e.g. the conversion rates or the ignition temperatures. With this purpose in mind, we can safely ignore most reaction steps and

limit our work to the investigation of the rate-limiting step, which in the case of methane is believed to be the abstraction of the first hydrogen from the molecule [105]. In the gas phase it takes 105 kcal/mol (4.56 eV/molecule) [106] to abstract one hydrogen from methane.

When the hydrogen abstraction occurs at a metal surface, both resulting H and CH<sub>3</sub> chemisorb on the surface upon dissociation (dissociative adsorption). There is an enthalpy barrier to be overcome for this reaction, even in the case that the dissociative adsorption is exothermic (i.e. it happens with release of energy). The height of this barrier determines the rate of the reaction. On the other hand, it has been established that on metallic surfaces the height of the enthalpy barrier is a linear function of the enthalpy of reaction [107], so that the problem of comparing catalytic activities for the dissociative adsorption of methane can be reduced to the calculation of enthalpy of reaction. Therefore we have in a first moment only calculated reaction energies for dissociative adsorption of methane on different surfaces, and only in a second step we have studied more in detail the dynamics of the reaction. This approach has the considerable advantage of being computationally less demanding, and therefore allows the investigation of a large variety of surfaces and phases. It is clear that surfaces where this first step of the oxidation is strongly endothermic, the reaction won't take place.

We have calculated reaction energies for dissociative adsorption of methane on a surface as

$$\Delta E = E_{CH_3} + E_H - 2 * E_{surf} - E_{meth} \quad (5.1)$$

where  $E_{CH_3}$  and  $E_H$  are the DFT-energies of slab with the respective radical adsorbed,  $E_{surf}$  the energy of the clean surface and  $E_{meth}$  the energy of the isolated methane molecule. A  $(2 \times 2)$  surface cell was used for every system. In all simulations full structural relaxations have been performed.

In table 5.1 we report results on energetics of dissociative adsorption of methane on the relevant surface systems.

On metallic platinum the reaction is more exothermic on Pt(100) than on Pt(111). Since on



System	Position of CH <sub>3</sub>	Position of H	$\Delta E$ (eV)	System	Position of CH <sub>3</sub>	Position of H	$\Delta E$ (eV)
Pt(111)	top	top	0.03	Pt(111)	top	FCC-hollow	-0.13
Pt(111)	FCC-hollow	top	0.59	Pt(111)	FCC-hollow	FCC-hollow	0.44
Pt(100)	top	top	-0.01	Pt(100)	top	bridge	-0.38
Pt(100)	bridge	top	-0.07	Pt(100)	bridge	bridge	-0.44
Pt <sub>3</sub> O <sub>4</sub> (100)	on Pt	on Pt	1.56	Pt <sub>3</sub> O <sub>4</sub> (100)	on Pt	on O	-0.46
Pt <sub>3</sub> O <sub>4</sub> (100)	on O	on Pt	0.18	Pt <sub>3</sub> O <sub>4</sub> (100)	on O	on O	-1.84
$\alpha$ -PtO <sub>2</sub> (0001)	on O	on O	2.03				
PtO-ML	on Pt	on Pt	0.74	PtO-ML	on Pt	on O	0.02
PtO-ML	on O	on Pt	0.89	PtO-ML	on O	on O	0.18
Pt <sub>3</sub> O <sub>4</sub> -ML	on O	on O	-1.47	Pt <sub>3</sub> O <sub>4</sub> -3ML	on O	on O	-1.87

Table 5.1:  $\Delta E$  for dissociative adsorption of methane. A negative value indicates an exothermic reaction.

metallic surfaces the height of the enthalpy barrier for dissociative adsorption of methane is a linear function of the reaction enthalpy with known linearity coefficients [107], we can estimate that barrier heights are 0.75 eV on Pt(111) and 0.47 eV on Pt(100). On Pt(111) CH<sub>3</sub> adsorbs preferentially on top of a Pt atom, so that the carbon atom reaches a tetrahedral coordination according to its sp<sup>3</sup> hybridization. C-Pt distance is 2.09 Å. On Pt(100) the preferred adsorption position of CH<sub>3</sub> is a bridge position, where C is bound to one Pt, one of the H atoms is bound to the other Pt and the C-H bond is stretched to 1.18 Å from the initial 1.10 Å in CH<sub>4</sub> (see fig. 5.1). Also in this configuration the C-Pt distance is 2.09 Å. It is not surprising that the reaction is energetically more favoured and the resulting radicals are more strongly bound on Pt(100); this is due to the fact that the Pt atoms of this surface are more undercoordinated than on Pt(111), and is consistent with the higher surface energy of Pt(100).

Calculations on platinum oxides show that adsorption behaviour strongly varies from one

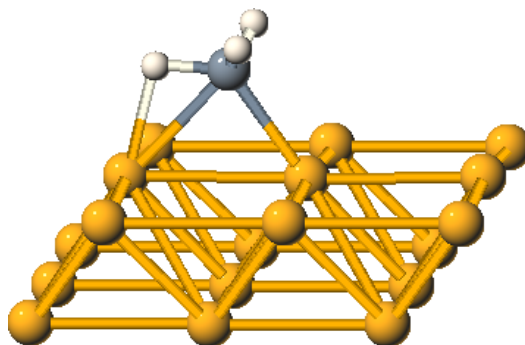


Figure 5.1:  $\text{CH}_3$  chemisorbed on  $\text{Pt}(100)$ .

oxide to the other.  $\text{Pt}_3\text{O}_4(100)$  is the bulk surface for which the reaction is most exothermic: not only does methane gain 1.84 eV by dissociatively adsorbing, but also both radicals adsorb on the undercoordinated surface oxygen, which might indicate an easier oxidation process. This is probably due to the peculiar position of the oxygens on this surface: they are bound only to two surface Pt atoms. On the other extreme, on  $\alpha\text{-PtO}_2(0001)$  the dissociation is very endothermic (2.03 eV), so that reaction is not expected to occur on this surface. This points to striking differences in adsorption behaviour and catalytic properties of these two phases, and leads to the idea that formation of  $\text{Pt}_3\text{O}_4$  should dramatically increase catalytic performance of platinum catalysts for oxidation reactions, while formation of  $\alpha\text{-PtO}_2$  should be connected to catalyst deactivation. This hypothesis is strengthened by our simulations of CO adsorption reported in the next section.

We have also investigated the effect of thin oxide films on the reactivity of platinum surfaces. Since on  $\text{Pt}(111)$  a monolayer of inert  $\alpha\text{-PtO}_2$  is the stable oxide monolayer, we have concentrated our attention on structures formed on  $\text{Pt}(100)$ . At monolayer level the stable structure at low temperature is the PtO-like monolayer (fig. 4.12(d)). On this structure dissociative adsorption of methane is not favoured, with a value of reaction energy of 0.02 eV, less exothermic than on the reduced  $\text{Pt}(100)$  surface. So on the stable oxide monolayers on both  $\text{Pt}(111)$  and  $\text{Pt}(100)$  dissociative adsorption of methane is energetically less favoured than on the clean metallic surfaces.

Since we have shown that as oxide growth progresses on  $\text{Pt}(100)$ , the thin film with  $\text{Pt}_3\text{O}_4$ -

like structure becomes thermodynamically more favourable, and at a thickness of three monolayers it is the dominant phase, we have calculated methane adsorption also on a model with three  $\text{Pt}_3\text{O}_4$  monolayers ( $\sim 1$  nm oxide) on Pt(100). On this system the energy gain for the dissociative adsorption of methane is 1.87 eV, a value close to that on the bulk  $\text{Pt}_3\text{O}_4$ . So a  $\sim 1$  nm thick  $\text{Pt}_3\text{O}_4$  film is not to be distinguished from a bulk  $\text{Pt}_3\text{O}_4$  as long as its interaction with methane is concerned.

By means of total energy calculations we have been able to make a first distinction between phases on which the reaction is very exothermic (like  $\text{Pt}_3\text{O}_4$ ) and those where the reaction is so endothermic that these phases can be characterized as inert (like  $\alpha\text{-PtO}_2$ ). In particular we have shown that on the most stable oxide monolayers on Pt(111) and Pt(100) dissociative adsorption of methane is not favoured in comparison to the metallic surface. We now turn to the first-principles molecular dynamics investigation of the dissociation reaction.

### 5.1.1 Dynamics of dissociation

We have studied the dynamics of the dissociation on the systems where the dissociative adsorption has proven to be energetically favoured, starting from the metallic Pt(111) surface as reference. To this purpose, we have simulated the trajectory of a methane molecule impinging on Pt(111) with an initial kinetic energy of 1 eV. Dissociation has not been observed on the clean regular surface (fig. 5.2). Then the same process has been simulated in the case of a methane molecule impinging on a Pt adatom on Pt(111), in presence of an oxygen atom to see if further steps of the oxidation process of methane could be observed after dissociation. On the adatom methane dissociates readily (fig. 5.4); the  $\text{CH}_3$  radical remains bound to the adatom, while the hydrogen has a tendency to form a OH group with the available oxygen. We have diminished systematically the initial kinetic energy and found that the dissociation takes place for an initial energy as low as 0.825 eV, while at 0.815 eV the methane hits the surface and bounces back in the gas phase without dissociating. Remarkably this value is very near to the height of the

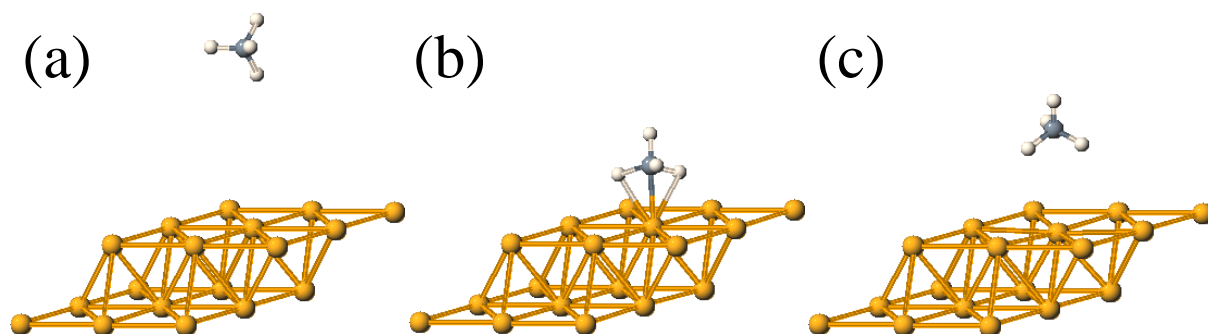


Figure 5.2: Snapshots of a methane molecule impinging on a regular Pt(111) surface with a kinetic energy of 1 eV. (a) Initial configuration. (b) After 44 fs of simulated time. (c) After 60 fs of simulated time.

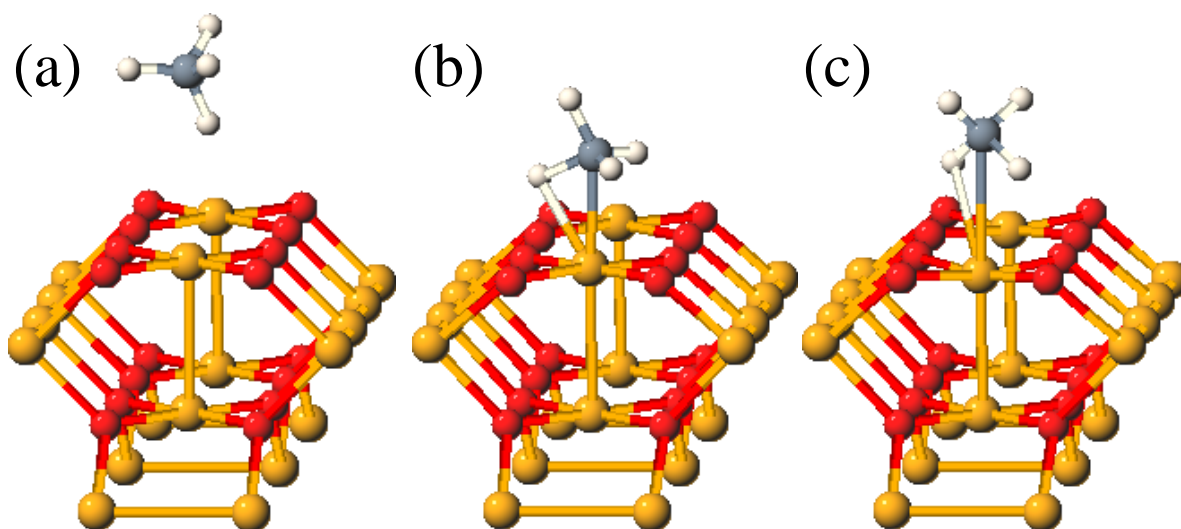


Figure 5.3: Snapshots of a methane molecule impinging on a regular  $\text{Pt}_3\text{O}_4(100)$  surface with a kinetic energy of 1 eV. (a) Initial configuration. (b) After 58 fs of simulated time. (c) After 75 fs of simulated time.

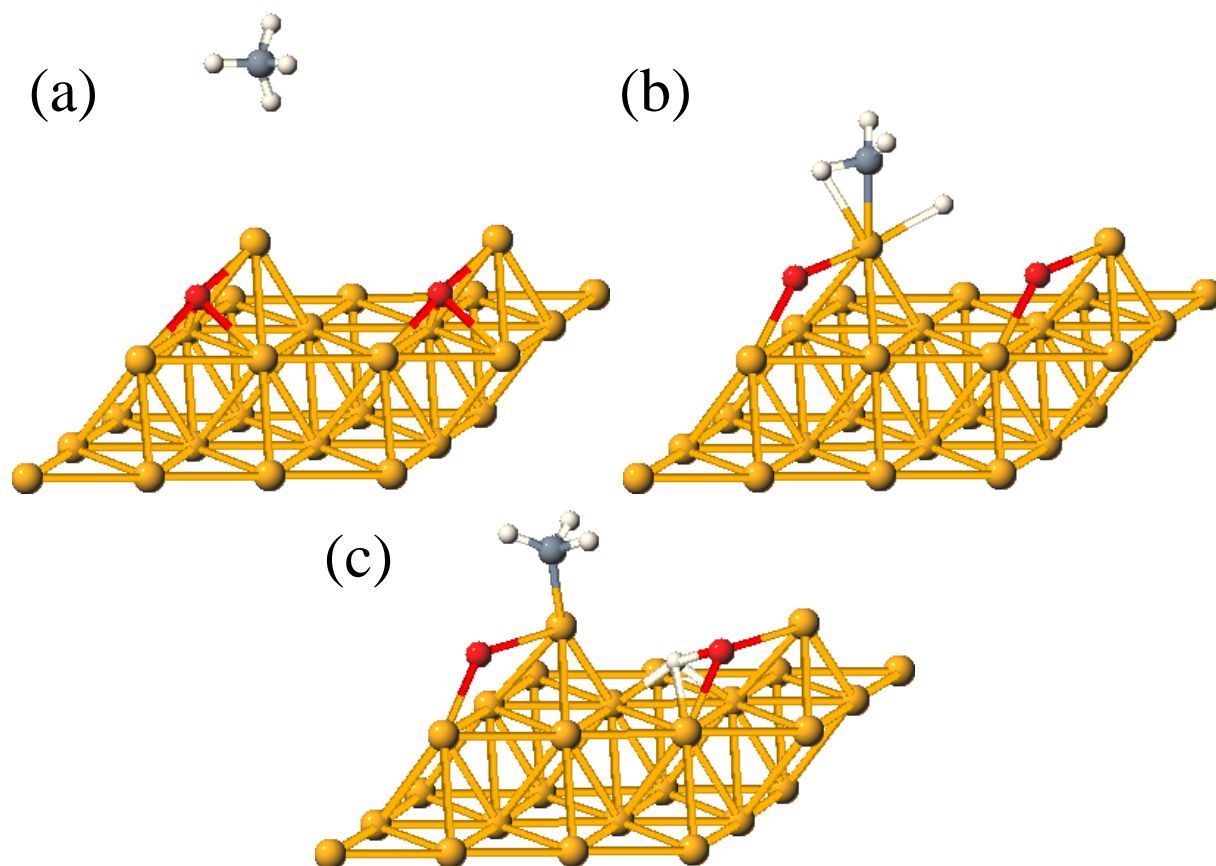


Figure 5.4: Snapshots of a methane molecule reacting with a Pt adatom on a Pt(111) surface with a kinetic energy of 1 eV. (a) Initial configuration. (b) After 53 fs of simulated time. (c) After 75 fs of simulated time.

enthalpy barrier of 0.75 eV estimated from reaction energy through the linear function of Michaelides et al. [107]. We note, however, that these two values should not be directly compared: the estimated enthalpy barrier is referred to the regular surface, while the value obtained from the simulation is only an upper bound for the barrier height on the system with the adatom.

Dissociation has not been observed on a regular  $\text{Pt}_3\text{O}_4(100)$  either (see fig. 5.3); a Pt adatom is again sufficient to observe dissociation at initial kinetic energy of 1 eV (see fig. 5.5). The same conclusions are drawn from the simulations of systems with an oxide monolayer on Pt(100): structures without adatoms, even if they have defects in form

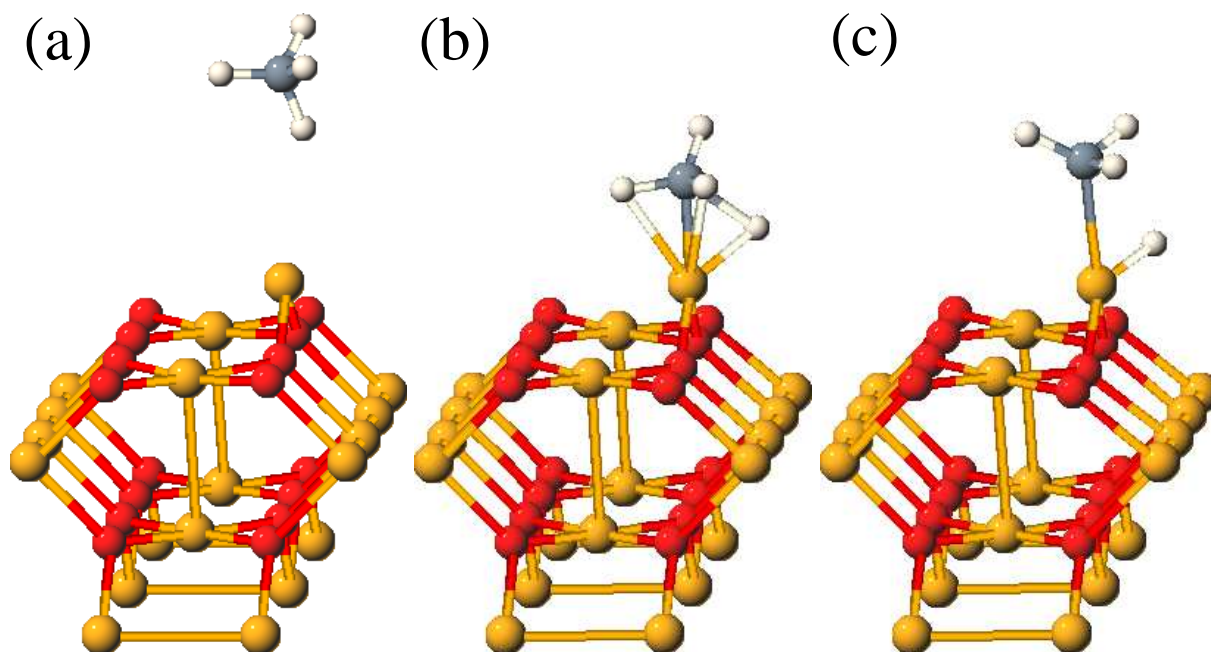


Figure 5.5: Snapshots of a methane molecule reacting with a platinum adatom on  $\text{Pt}_3\text{O}_4(100)$  with a kinetic energy of 1 eV. (a) Initial configuration. (b) After 53 fs of simulated time. (c) After 65 fs of simulated time.

of vacancies (see fig. 5.6 and 5.7), are not apt to dissociate methane, while adatoms are sufficient to induce the dissociation (see fig. 5.8). The heavily undercoordinated Pt adatom is clearly a site which favours the dissociation, because of its strong tendency to saturate the dangling bonds via hybridization with the impinging molecule in a process which leads to activation and dissociation of a C-H bond at sufficiently high kinetic energy.

## 5.2 CO oxidation

CO is oxidized in presence of platinum at temperatures as low as 350 K [108]. The actual mechanism of the oxidation depends on the process conditions, and switches from a Langmuir-Hinshelwood mechanism at low oxygen pressures to a Mars-Van Krevelen mechanism at high oxygen pressures [8], depending on the oxidation state of the platinum surface.

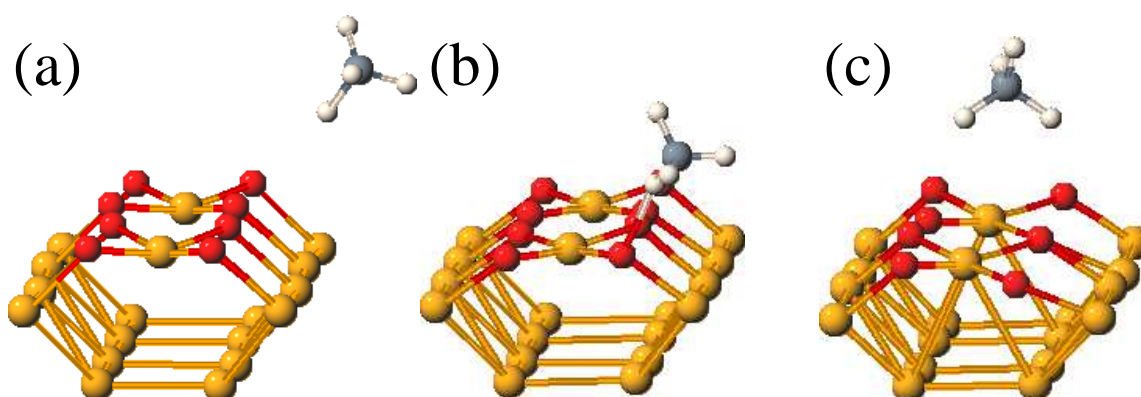


Figure 5.6: Snapshots of a methane molecule impinging on a  $\text{Pt}_3\text{O}_4$ -like monolayer on Pt(100) with a kinetic energy of 1 eV. Moreover one C-H is stretched in the starting configuration (a) Initial configuration. (b) After 36 fs of simulated time. (c) After 75 fs of simulated time.

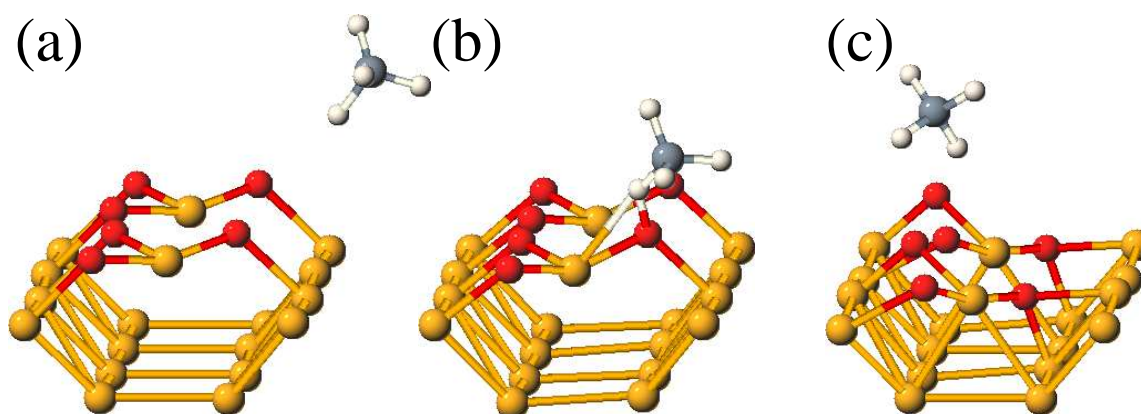


Figure 5.7: Snapshots of a methane molecule impinging on an oxygen vacancy on a  $\text{Pt}_3\text{O}_4$ -like monolayer on Pt(100) with a kinetic energy of 1 eV. Moreover one C-H is stretched in the starting configuration (a) Initial configuration. (b) After 31 fs of simulated time. (c) After 75 fs of simulated time.

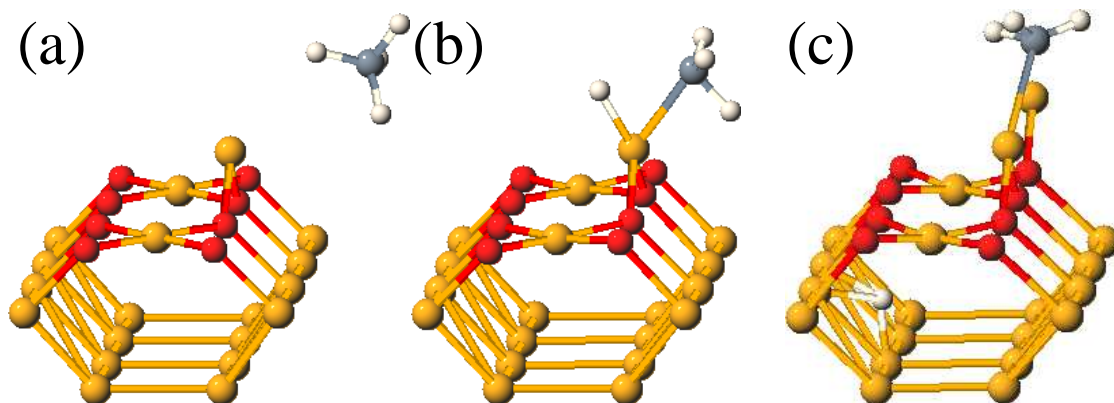


Figure 5.8: Snapshots of a methane molecule reacting with a platinum adatom on a  $\text{Pt}_3\text{O}_4$ -like monolayer on  $\text{Pt}(100)$  with a kinetic energy of 1 eV. Moreover one C-H is stretched in the starting configuration (a) Initial configuration. (b) After 34 fs of simulated time. (c) After 68 fs of simulated time.

In a first step, we have considered the adsorption process of CO on the relevant bulk surfaces. In a second step we have turned our attention to the height of the barrier for CO oxidation on  $\text{Pt}_3\text{O}_4(100)$ . Finally, we have taken a deeper look at the conditions under which the oxidation-reduction cycle of the oxide surface can really take place and be stable against deactivation or complete oxide reduction.

As reference we have calculated CO adsorption on  $\text{Pt}(111)$ . These calculations are particularly delicate, since this is one of the few known cases where DFT incorrectly predicts the favourite adsorption site. On  $\text{Pt}(111)$  we have found CO to adsorb preferentially on FCC-hollow position with an adsorption energy of 1.94 eV, versus 1.90 eV on bridge position between two Pt atoms and 1.86 eV on top of a Pt atom. These results are in contradiction with the experimental finding that the adsorption in a 'on top' position is energetically more favoured, but in agreement with other DFT calculations [109]. This discrepancy has been thoroughly discussed [110] and it is due to the small difference (in the order of 0.1 eV) in adsorption energies among the different sites. We can therefore assume here that a comparison among adsorption energy values between different phases is meaningful when the energy differences are larger than a few tenths of 1 eV.



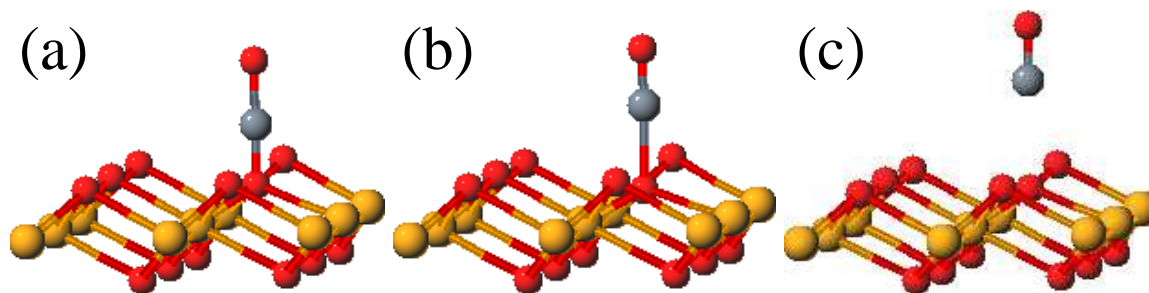


Figure 5.9: Snapshots of a CO molecule desorbing from an  $\alpha$ -PtO<sub>2</sub>(0001). (a) After 7 fs of simulated time. (b) After 15 fs of simulated time. (c) After 73 fs of simulated time.

We have then turned our attention to the two relevant bulk oxide surfaces: Pt<sub>3</sub>O<sub>4</sub>(100) and  $\alpha$ -PtO<sub>2</sub>(0001). The stunning result is that for CO evidence of dramatically different catalytic behaviour between Pt, Pt<sub>3</sub>O<sub>4</sub> and  $\alpha$ -PtO<sub>2</sub> is even more overwhelming than in the case of methane, and that simulations confirm the idea that Pt<sub>3</sub>O<sub>4</sub> is the most active phase for catalysis of oxidation reactions. No adsorption of CO molecules have been observed on the  $\alpha$ -PtO<sub>2</sub>(0001) or the Pt<sub>3</sub>O<sub>4</sub>(100) surfaces. Several structural minimisation attempts of the CO molecule near the  $\alpha$ -PtO<sub>2</sub>(0001) surface led to spontaneous *desorption* of CO (fig. 5.9). This result, combined with the endothermic methane dissociation reaction described in the previous section, confirms that this oxide structure is rather inert as far as oxidation reactions of combustion exhausts are concerned. On the contrary, Pt<sub>3</sub>O<sub>4</sub> is once again revealed to be extremely active towards catalytic oxidation. Namely, several attempts of structural minimisation of CO molecules adsorbed on the Pt<sub>3</sub>O<sub>4</sub>(100) surface resulted in spontaneous desorption of CO<sub>2</sub> molecules (fig. 5.10). In this reaction, CO binds strongly to one of the four undercoordinated oxygen atoms of the surface, while the bonds between this O atom and the underlying Pt atoms break. So the investigation of CO behaviour brings strong support to the finding that Pt<sub>3</sub>O<sub>4</sub> is by far the Pt oxide with the best catalytic properties for oxidation reactions of uncombusted carbon compounds.

The different behaviour is to be brought in relation with the principle of Sabatier [111], which relates the activity of a compound for catalytical oxidation to the binding energy

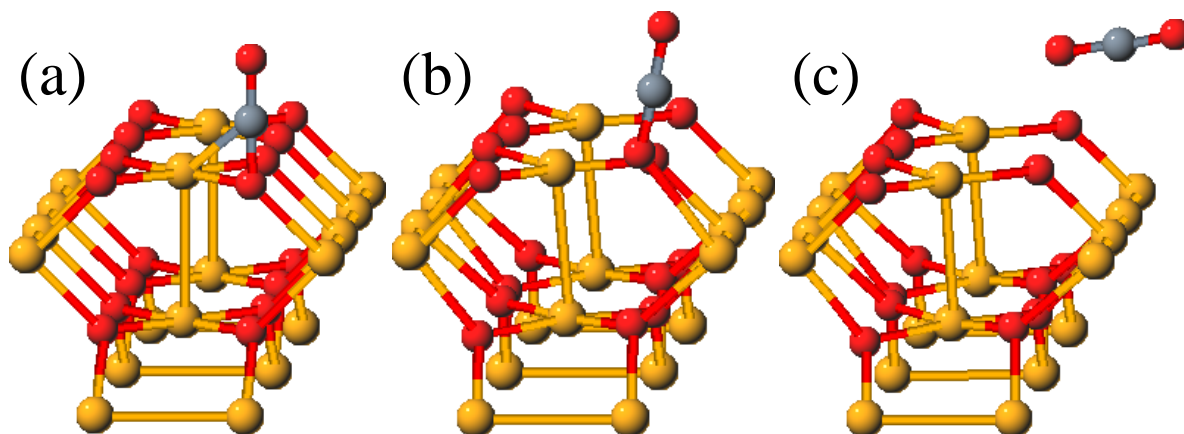


Figure 5.10: Snapshots of a CO molecule oxidizing on  $\text{Pt}_3\text{O}_4(100)$ . (a) Initial configuration. (b) After 239 fs of simulated time. (c) After 409 fs of simulated time.

of the oxygen atoms on it (or equivalently to the energy necessary to create an oxygen vacancy). This must be moderate, roughly between +2 eV and -2 eV with respect to the isolated oxygen molecule (see fig. 2 in Ref. [28]): if it is too low, the oxygen molecule from the gas doesn't react with the surface in the first place; if the oxygen is too strongly bound to the surface (more than  $\sim 2$  eV/O atom), it cannot be released to participate in the oxidation of the incoming molecules. On  $\text{Pt}_3\text{O}_4(100)$  the energy necessary to create an oxygen vacancy on the surface is +1.69 eV (similar to the binding energy of an O atom on Pt(111) at a coverage of 0.25 ML), while on  $\alpha\text{-PtO}_2(0001)$  it amounts to +2.38 eV. This energy is the difference between the DFT total energy of the regular surface and that of the surface with an oxygen vacancy plus half of the energy of an isolated oxygen molecule. The rate-limiting step for CO oxidation on this surface is the approach of a CO molecule from the gas phase and the formation of an initial bond with the surface. To compute the enthalpy barrier associated with this process, a series of total energy calculations have been performed decreasing the distance between the C atom of the CO molecule and an O atom of the surface. At every step the geometry of the whole system is fully minimised keeping fixed the  $C_{\text{CO}}\text{-O}_{\text{surf}}$  distance. The results are reported in fig. 5.11, and show that the maximum enthalpy barrier for CO binding to the surface and formation of  $\text{CO}_2$  is as

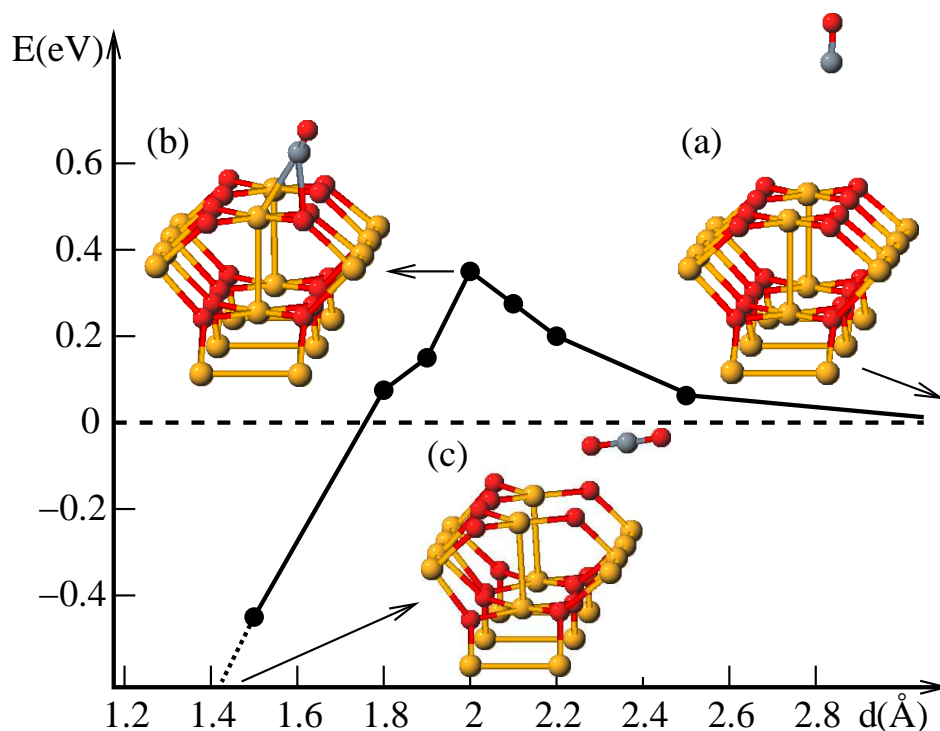


Figure 5.11: Barrier for CO oxidation on  $\text{Pt}_3\text{O}_4(100)$ . On the x-axis the distance  $d(\text{C}-\text{O}_{surf})$  (in Å) is plotted, on the y-axis the energy (in eV). (a) The CO molecule is far from the surface ( $d(\text{C}-\text{O}_{surf})=5$  Å); the energy of this configuration has been chosen as zero-level; (b) transition state ( $d(\text{C}-\text{O}_{surf})=2$  Å); (c) desorbed  $\text{CO}_2$  molecule. The energy of the final state lies 1.49 eV lower than that of the initial state plotted in (a).

low as 0.34 eV. This is in particular a much lower value than the typical barriers of more than about 0.7 eV which characterise the Langmuir-Hinshelwood reaction of CO oxidation on clean Pt surfaces [112, 113].

### 5.2.1 Energy balance of the Mars-Van Krevelen mechanism

We have shown that CO oxidation may follow a Mars-Van Krevelen mechanism on  $\text{Pt}_3\text{O}_4$ . The Mars-Van Krevelen mechanism relies on a balance between an oxidized and a partly reduced state between which the surface can switch easily. For this mechanism to be

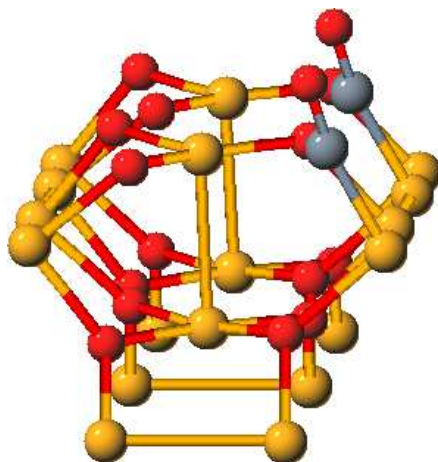


Figure 5.12: CO in an O-vacancy on  $\text{Pt}_3\text{O}_4$ .

effective, two conditions are necessary: 1) the oxygen on the surface must be bound loosely enough to be released in presence of the species that must be oxidized; 2) after release of oxygen, the partly reduced surface must have the tendency to return to its initial oxidized state and to close the catalytic cycle. If condition 1) is not fulfilled, the oxide will be rather inactive for the heterogenous catalytic oxidation reaction, or at least it will not follow this mechanism. If condition 2) is not fulfilled, the oxide will have a tendency to be either poisoned or reduced to a purely metallic state (see also fig. 2.2), and the considered oxide phase will be of no relevance for the steady state of the heterogenous catalytic oxidation reaction. The two conditions are related to the principle of Sabatier explained in the previous section.

The simulations of CO on  $\text{Pt}_3\text{O}_4$  show clearly that the oxygens are loose enough to react with the CO molecule. It remains to be seen if the binding energy of the oxygen is high enough for the system to reoxidize also in presence of CO. For the CO oxidation on  $\text{Pt}_3\text{O}_4(100)$  we have calculated the energy of the relevant states of the surface during a Mars-Van Krevelen cycle, to see whether, or under which circumstances, condition 2) is fulfilled. At first we have considered a CO adsorbed in an O-vacancy on the surface (fig. 5.12). This corresponds to having the active site poisoned by CO, which hinders the reoxidation of the surface. Then we have considered a CO adsorbed on an oxygen

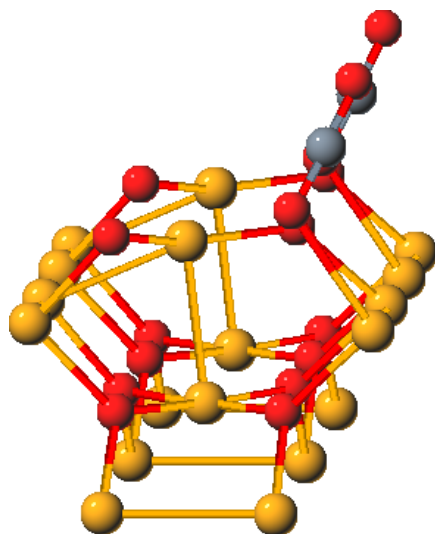


Figure 5.13: CO adsorbed on a partially reduced  $\text{Pt}_3\text{O}_4$ .

on the partly reduced surface (fig. 5.13); this is the first step towards further reduction of the surface. For these systems we have calculated the difference in Gibbs' free energy with respect to the regular reoxidized surface (fig. 4.12(a)). To do this we have taken into account the enthalpy and entropy contributions of both the CO [114] and the  $\text{O}_2$  [42] gases at 1 atm pressure, and have extended them to a wide range of pressures by treating them as ideal gases, for which  $\mu(p) = \mu(p_0) + 1/2 k T \ln(p/p_0)$  [5] ( $\mu$  is the chemical potential of the gaseous species). In fact, the poisoned state (fig. 5.12) lies 0.23 eV higher in energy than the state in fig. 5.13, and this energy difference does not depend on either the temperature or the pressure, since the two states have the same composition and (T,p) dependence enters in our model only through the chemical potentials of  $\text{O}_2$  and CO. Therefore the poisoned state never appears in the phase diagram of the system, depicted in fig. 5.14. It is clear that reoxidation is preferred over both further reduction and poisoning through CO, unless CO pressure is at least two order of magnitude larger than oxygen pressure; therefore it is probable that a Mars-Van Krevelen mechanism is expected to take place on this kind of active site.

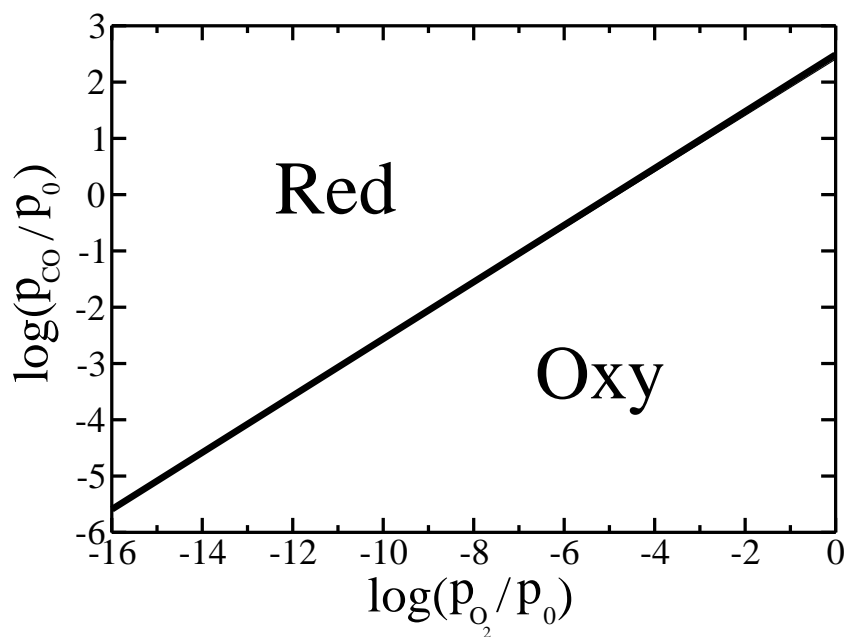


Figure 5.14: Relative stability regions of two different states of the  $Pt_3O_4(100)$  surface at 400 K, in dependence of CO and  $O_2$  pressures: CO adsorbed on an oxygen on the partially reduced surface (**Red**, see fig. 5.13) and a regular  $Pt_3O_4(100)$  (**Oxy**, see fig. 4.12(a)).  $p_0 = 1$  atmosphere.

# Chapter 6

## Conclusions

### 6.1 Summary

It is well established that platinum can form different oxides under oxygen-rich conditions, but no existing study linked the formation of a well characterized oxide phase to changes in catalytic properties towards oxidation of both methane and CO. In this thesis we have calculated the thermodynamic stability of possible oxide structures and simulated the dissociative adsorption of methane and the oxidation of carbon monoxide on them. We have found that at atmospheric pressures two bulk Pt oxides are stable at different temperatures:  $\alpha$ -PtO<sub>2</sub> at low temperature and Pt<sub>3</sub>O<sub>4</sub> at higher temperature. In particular, the employed first-principles thermodynamics approach reveals a region of thermodynamic stability of bulk Pt<sub>3</sub>O<sub>4</sub> between 870 K and 974 K in 1 atm of oxygen partial pressure. These values agree with the observation that  $\alpha$ -PtO<sub>2</sub> decomposes in air above 870 K [20].

Since in technologically relevant applications in catalysis platinum is present in form of clusters, we have calculated how the bulk phase diagram is modified when oxidized Pt particles of finite size are taken into account. We have determined surface energy contributions and form of metallic Pt clusters and of Pt<sub>3</sub>O<sub>4</sub> clusters by Wulff's construction. For Pt we have obtained clusters in form of irregular truncated octahedrons; 14% of the surface is Pt(100), the rest is Pt(111). For Pt<sub>3</sub>O<sub>4</sub> we have considered the (100) and (110)

surfaces. It turns out that the surface energy of the surface with (110) orientation is too high, and Wulff's clusters of  $\text{Pt}_3\text{O}_4$  are cubes with only (100) surfaces. Surface free energy of  $\alpha\text{-PtO}_2(0001)$  is only  $2 \text{ meV}/\text{\AA}^2$ , so that we have taken the isolated O-Pt-O trilayer as  $\alpha\text{-PtO}_2$  'cluster'. We have considered a metallic cluster and compared its Gibbs' free energy to that of  $\text{Pt}_3\text{O}_4$  and  $\alpha\text{-PtO}_2$  clusters with the same number of Pt atoms. The region of stability of  $\text{Pt}_3\text{O}_4$  shrinks and shifts to higher temperatures with respect to the phase diagram of bulk phases (fig. 4.11) as the diameter of the cluster diminishes, the region of stability of  $\alpha\text{-PtO}_2$  expands to higher temperatures (see fig. 4.17).

While bulk oxide phases are thermodynamically stable, it is common knowledge that platinum does not undergo spontaneous oxidation at low temperatures. We have therefore also considered that oxidation might be kinetically hindered, so that only thin oxide films on platinum surfaces form. On Pt(111) an  $\alpha\text{-PtO}_2$  monolayer (ML) is the most stable ML-phase. On this oxide phase CO desorbs without noticeable barrier, and dissociative adsorption of methane is extremely endothermic; we therefore expect  $\alpha\text{-PtO}_2$  to be a very poor catalyst for oxidation of these species. Gélin et al. [115] report about a dispersed  $\text{PtO}_2$  phase less reactive towards methane oxidation; Yazawa and co-workers [116] find a correlation between low activity of platinum for propane oxidation and  $\text{PtO}_2$  presence. On the other hand,  $\text{PtO}_2$  is known to act as a potent catalyst for hydrosilylation and oxidation of ethanol in liquid phase [71, 117]. It is assumed that the oxidation of the substrates causes a reduction of the oxide to metallic platinum according to mechanisms which are not identified to date, and could possibly involve the presence of oxygen vacancies [71]. On Pt(100) there are two competing structures, a PtO-like and a  $\text{Pt}_3\text{O}_4$ -like. The PtO-like monolayer is energetically favoured over the  $\text{Pt}_3\text{O}_4$ -like monolayer, and it displays poor adsorption properties for methane. As a consequence, we can draw the fundamental conclusion that stable and defect-free oxide monolayers on both Pt(111) and Pt(100) are detrimental to dissociative adsorption of methane. Since  $\text{Pt}_3\text{O}_4$  can grow epitaxially on Pt(100) (strain smaller than 1%), while the PtO-like structure is compressed by 9% in one direction and strained 4% in the other on Pt(100), at growing oxide film thickness the PtO-like film becomes more and more unfavourable, and at level of three oxide-monolayers the  $\text{Pt}_3\text{O}_4$



oxide is more stable than the other up to  $\sim 1250$  K. So, in case of oxide films grown on Pt(100),  $\text{Pt}_3\text{O}_4$  with (100) surface orientation is expected to be the thermodynamically favoured structure. Adsorption of  $\text{CH}_4$  on three monolayers  $\text{Pt}_3\text{O}_4$  ( $\sim 1$  nm thickness) on Pt(100) is exothermic by 1.87 eV, a value higher than on any other system considered, which is practically identical to that on the bulk  $\text{Pt}_3\text{O}_4(100)$  surface.

Indeed, of all systems considered,  $\text{Pt}_3\text{O}_4(100)$  is the best surface for oxidative reactions: a CO has to overcome a barrier of only 0.34 eV to react with surface oxygen, it readily takes the oxygen away from the regular surface and desorbs without noticeable barrier as  $\text{CO}_2$  into the gas phase; methane not only dissociates with an adsorption energy of 1.84 eV, but also both radicals adsorb on the undercoordinated surface oxygens. The oxidation of a CO molecule on the  $\text{Pt}_3\text{O}_4(100)$  surface creates an oxygen vacancy on the surface. From this state we have taken in consideration three different directions the system can evolve into: either the oxygen vacancy is occupied again by an oxygen atom, thereby closing the catalytic cycle, or it is occupied by a CO molecule (overlooking the presence of other chemical species), thereby poisoning the active site, or further CO oxidation takes place, leading to further reduction of the surface. It is clear that the first direction must be favoured for this oxide surface to exist and be catalytically active. We have therefore compared the Gibbs' free energies of the regular oxidized surface, that of the partially reduced surface with a CO adsorbed in the O-vacancy (poisoned state) and that of the partially reduced surface with a CO adsorbed on an oxygen (which is the first step towards further reduction of the surface), to see under which partial pressures of CO and  $\text{O}_2$  the closing of the catalytic cycle is favoured. The phase diagram for these states, reported in fig. 5.14, has led us to the conclusion that the reoxidation back to the initial state is favoured over the other possibilities unless the CO pressure is at least a couple of orders of magnitude larger than the  $\text{O}_2$  pressure, and that therefore  $\text{Pt}_3\text{O}_4(100)$  is expected to work effectively as oxidation catalyst under oxygen-rich conditions with a Mars-Van Krevelen mechanism involving surface reduction and reoxidation.

## 6.2 Future works

Summarizing, in this thesis we have evaluated the reactivity of platinum oxides for dissociative adsorption of methane and CO oxidation, shown that  $\text{Pt}_3\text{O}_4$  should be the most active phase for these reactions and predicted thermodynamic stability of this phase in bulk form in a region around 900 K (between 870 K and 974 K at 1 atm oxygen partial pressure), region that shrinks and moves to higher temperatures for clusters smaller than 20 nm. While we have found that, whenever experimental data are available, our predictions have been confirmed with satisfactory precision, more experiments are necessary, in particular to assess stability and catalytical activity of  $\text{Pt}_3\text{O}_4$ . Even though more stringent tests of our theory are still missing, we would like to formulate proposals based on  $\text{Pt}_3\text{O}_4$  formation to improve catalyst performance. Since oxidation of CO takes place at temperatures as low as 350 K [108], one would like to produce  $\text{Pt}_3\text{O}_4$  and then keep it as metastable state at the working conditions. One might obtain  $\text{Pt}_3\text{O}_4$  by a heat treatment on metallic clusters at the temperatures at which this oxide is stable. For this method to be effective one needs clusters of intermediate size: for clusters smaller than 5 nm, the  $\text{Pt}_3\text{O}_4$  is stable only at temperatures higher than  $\sim 1050$  K, at which considerable sintering is expected; clusters larger than 20 nm have probably a too low specific surface, so that much of the platinum is in the inside and not available for the catalysis. Moreover, cluster size distribution must be narrow, since the stability region of  $\text{Pt}_3\text{O}_4$  is strongly temperature dependent, so that clusters with very different sizes may oxidize to different phases (see fig. 4.17). Another important conclusion of this thesis is that  $\text{Pt}_3\text{O}_4$  can grow epitaxially on Pt(100), a property that could be exploited to control oxide growth. Experiments are currently under way at the TASC Laboratory in Trieste to analyze initial steps of the oxidation of Pt(100). Experiments are under way at the TU Dresden and at the TU Freiberg to test which phases form in Pt clusters treated at different temperatures, and how this correlates with catalytical activity. In particular it would be interesting to investigate the effect of sodium on stability and catalytical properties of  $\text{Pt}_3\text{O}_4$ , since existence of  $\text{Na}_x\text{Pt}_3\text{O}_4$  ( $0 \leq x \leq 1$ ), isostructural to  $\text{Pt}_3\text{O}_4$ , is well known (so that  $\text{Pt}_3\text{O}_4$  is sometimes referred to as 'sodium-

free  $\text{Na}_x\text{Pt}_3\text{O}_4$  [22]).

Investigating stability and chemical properties of  $\text{Na}_x\text{Pt}_3\text{O}_4$  could also be done with the simulation methods employed in this thesis. Other open questions that could be addressed by first-principles methods are the role of poisoning species such as sulphur and chlorine, the effects of the ceramic support (e.g.  $\gamma\text{-Al}_2\text{O}_3$ ) on the chemical properties of the cluster, the effects of the presence of other transition metals such as rhodium and palladium on platinum. First-principles methods could also be employed together with other techniques such as Monte Carlo methods to gain insight into processes that are of paramount importance, but take place on time scales which are too large to be simulated by first-principles methods alone: kinetics of the reaction on the cluster surface and cluster sintering.



# Bibliography

- [1] Data of the United Nations Conference on Trade and Development, <http://r0.unctad.org/infocomm/>
- [2] Li, W.-X.; Stampfl, C.; Scheffler, M. *Phys. Rev. B* **2003**, *67*, 45408.
- [3] Li, W.-X.; Stampfl, C.; Scheffler, M. *Phys. Rev. B* **2003**, *68*, 165412.
- [4] Lundgren, E.; Gustafson, J.; Mikkelsen, A.; Andersen, J. N.; Stierle, A.; Dosch, H.; Todorova, M.; Rogal, J.; Reuter, K.; Scheffler, M. *Phys. Rev. Lett.* **2004**, *92*, 46101.
- [5] Reuter, K.; Scheffler, M. *Phys. Rev. B* **2001**, *65*, 35406.
- [6] Reuter, K.; Scheffler, M. *Phys. Rev. Lett.* **2003**, *90*, 46103.
- [7] Bergermayer, W.; Schweiger, H.; Wimmer, E. *Phys. Rev. B* **2004**, *69*, 195409.
- [8] Hendriksen, B.; Frenken, J. *Phys. Rev. Lett.* **2002**, *89*, 046101.
- [9] Li W. X.; Österlund L.; Vestergaard E. K.; Vang R. T.; Matthiesen J.; Pedersen T. M.; Lægsgaard E.; Hammer B.; Besenbacher F. *Phys. Rev. Lett.* **2004**, *93*, 146104.
- [10] Li, W. X.; Hammer, B. *Chem. Phys. Lett.* **2005**, *409*, 1.
- [11] Petroski J. M.; Wang Z. L.; Green T. C.; El-Sayed M. A. *J. Phys. Chem. B* **1998**, *102*, 3316.
- [12] Hodnett, B. K.; *Heterogeneous catalytic oxidation*, John Wiley & Sons Ltd., Chichester, 2000.

- [13] Walker, A. P., *Topics in Catal.* **2004**, *28*, 165.
- [14] Alzueta, M. U.; Glarborg, P. *Environ. Sci. Technol.* **2003**, *37*, 4512.
- [15] Bertram, M.; Beta, C.; Pollmann, M.; Mikhailov, A. S.; Rotermund, H. H.; Ertl, G. *Phys. Rev. B* **2003**, *67*, 36208.
- [16] Over, H.; Kim, Y. D.; Seitsonen, A. P.; Wendt, S.; Lundgren, E.; Schmid, M.; Varga, P.; Morgante, A.; Ertl, G. *Science* **2000**, *287*, 1474.
- [17] Langmuir, I. *J. Am. Chem. Soc.* **1918**, *40*, 1361.
- [18] Mallens E. P. J.; Hoebink J. H. B. J.; Marin G. B. *Catal. Lett.* **1995**, *33*, 291.
- [19] Ackermann, M. D.; Pedersen, T. M.; Hendriksen, B. L. M.; Robach, O.; Bobaru, S. C.; Popa, I.; Quiros, C.; Kim, H.; Hammer, B.; Ferrer, S.; Frenken, J. W. M. *Phys. Rev. Lett.* **2005**, *95*, 255505.
- [20] Rothschild, W. G.; Yao, H. C.; Plummer, H. K. Jr. *Langmuir* **1986**, *2*, 588.
- [21] Lundgren, E.; Kresse, G.; Klein, C.; Borg, M.; Andersen, J. N.; De Santis, M.; Gauthier, Y.; Konvicka, C.; Schmid, M.; Varga, P. *Phys. Rev. Lett.* **2002**, *88*, 246103.
- [22] Muller O.; Roy R. *J. Less-Common Metals* **1968**, *16*, 129.
- [23] Moore, W. J., Jr.; Pauling, L. *J. Am. Chem. Soc.* **1941**, *63*, 1392.
- [24] Punnoose, A.; Seehra, M. S.; Wender, I. *Fuel Process. Technol.* **2001**, *74*, 33.
- [25] Wang C.-B.; Lin H.-K.; Hsu S.-N.; Huang T.-H.; Chiu H.-C. *J. Mol. Catal.* **2002**, *188*, 201.
- [26] Galloni E. E.; Roffo A. E. *J. Chem. Phys.* **1941**, *9*, 875.
- [27] Tang H.; Van der Ven A.; Trout B. L. *Phys. Rev. B* **2004**, *70*, 45420.
- [28] Gong X.-Q.; Raval R.; Hu P. *Phys. Rev. Lett.* **2004**, *93*, 106104.

- [29] Payne M. C.; Teter M. P.; Allan D. C.; Arias T. A.; Joannopoulos J. D. *Rev. Mod. Phys.* **1992**, *64*, 1045.
- [30] Galli, G.; Pasquarello, A.; in *Computer simulation in chemical physics*; Allen, M. P., Tildesley, D. J., Eds.; Kluwer Academic Publishers: 1993; 261.
- [31] Car R.; Parrinello M. *Phys. Rev. Lett.* **1985**, *55*, 2471.
- [32] Hohenberg, P.; Kohn, W. *Phys. Rev. B* **1954**, *136*, B864.
- [33] Kohn, W.; Sham, L. J. *Phys. Rev. B* **1965**, *140*, A1130.
- [34] Perdew, J. P.; Wang, Y. *Phys. Rev. B* **1976**, *13*, 4274.
- [35] De Vita, A.; Canning, A.; Car, R. *EPFL Supercompt. J.* **1994**, *6*, 22.
- [36] Stengel, M.; De Vita, A. *Phys. Rev. B* **2000**, *62*, 15283.
- [37] Pastore, G.; Smargiassi, E.; Buda, F. *Phys. Rev. A* **1991**, *44*, 6334.
- [38] Ceperley, D. M.; Alder, B. J. *Phys. Rev. Lett.* **1980**, *45*, 566.
- [39] Perdew, J. P.; Burke, K.; Ernzerhof, M. *Phys. Rev. Lett.* **1996**, *77*, 3865; **1997**, *78*, 1396(E).
- [40] Troullier, N.; Martins, J. L. *Phys. Rev. B* **1991**, *43*, 1993.
- [41] Vanderbilt, D. *Phys. Rev. B* **1990**, *41*, 7892.
- [42] Otto, J.; Thomas, W.; in *Landolt-Börnstein*, 6th edition; Hausen H., Ed; Springer-Verlag: Berlin, 1967; vol IV/4a, pp 230-231.
- [43] Giannozzi P.; de Gironcoli S.; Pavone P.; Baroni S. *Phys. Rev. B* **1991**, *43*, 7231.
- [44] Gonze, X. *Phys. Rev. B* **1997**, *55*, 10337.
- [45] Gonze, X.; Lee, C. *Phys. Rev. B* **1997**, *55*, 10355.

- [46] Lee, C.; Gonze, X. *Phys. Rev. B* **1995**, *51*, 8610.
- [47] Ghosez, Ph.; Michenaud, J.-P.; Gonze, X. *Phys. Rev. B* **1998**, *58*, 6224.
- [48] Posternak, M.; Baldereschi, A.; Resta, R.; Krakauer, H. *Phys. Rev. B* **1997**, *55*, R15983.
- [49] Posternak, M.; Resta, R.; Baldereschi, A. *Phys. Rev. B* **1994**, *50*, 8911.
- [50] King-Smith, R. D.; Vanderbilt, D. *Phys. Rev. B* **1993**, *47*, 1651.
- [51] Bengone, O.; Alouani, M.; Blöchl, P.; Hugel, J. *Phys. Rev. B* **2000**, *62*, 16392.
- [52] Cococcioni, M.; de Gironcoli, S. *Phys. Rev. B* **2005**, *71*, 35105.
- [53] Anisimov, V. I.; Zaanen, J.; Andersen, O. K. *Phys. Rev. B* **1991**, *44*, 943.
- [54] Anisimov, V. I.; Aryasetiawan, F.; Lichtenstein, A. I. *J. Phys.: Condens. Matter*, **1997**, *9*, 767.
- [55] Baroni, S.; Dal Corso, A.; de Gironcoli, S.; Giannozzi, P.; Cavazzoni, C.; Ballabio, G.; Scandolo, S.; Chiarotti, G.; Focher, P.; Pasquarello, A.; Laasonen, K.; Trave, A.; Car, R.; Marzari, N.; Kokalj, A. <http://www.pwscf.org/>
- [56] Bader, R. F. W.; *Atoms in molecules: a quantum theory*; Clarendon: Oxford, 1990.
- [57] Colombi Ciacchi, L.; Pompe, W.; De Vita A. *J. Am. Chem. Soc.* **2001**, *123*, 7371.
- [58] Monkhorst H. J.; Pack J. D. *Phys. Rev. B* **1976**, *13*, 5188.
- [59] Ashcroft, N. W.; Mermin, N. D. *Solid State Physics*; Saunders College Publishing: Philadelphia, 1976.
- [60] Boisvert, G.; Lewis, L. J.; Scheffler, M. *Phys. Rev. B* **1998**, *57*, 1881.
- [61] Kaye, G. W. C.; Laby, T. H.; *Tables of physical and chemical constants*, 16th edition; Longman Group: Burnt Mill, 1995; p 45.



- [62] The ABINIT code is a common project of the Universit Catholique de Louvain, Corning Incorporated, and other contributors (URL <http://www.abinit.org>); Gonze, X. et al. *Comput. Mater. Sci.* **2002**, *25*, 478.
- [63] Singh, N.; Banger, N. S.; Singh, S. P. *Phys. Rev. B* **1988**, *38*, 7415.
- [64] Li, M.; Goddard III, W. A. *Phys. Rev. B* **1989**, *40*, 12155.
- [65] McBride, J. R.; Graham, G. W.; Peters, C. R.; Weber, W. H. *J. Appl. Phys.* **1991**, *69*, 1596.
- [66] Reprinted from *J. Less-Common Metals*, Vol. 16; Authors: O. Muller, R. Roy; 'Formation and stability of the platinum and rhodium oxides at high oxygen pressures and the structures of Pt<sub>3</sub>O<sub>4</sub>,  $\beta$ -PtO<sub>2</sub> and RhO<sub>2</sub>'; p. 133; copyright 1968, with permission from Elsevier.
- [67] Hasegawa, M.; Nishidate, K. *Phys. Rev. B* **2004**, *70*, 205431.
- [68] Baskin, Y.; Meyer, L. *Phys. Rev.* **1955**, *100*, 544.
- [69] Weber, W. H.; Graham, G. W.; McBride, J. R. *Phys. Rev. B* **1990**, *42*, 10969.
- [70] Wu, R.; Weber, W. H. *J. Phys.: Condens. Matter* **2000**, *12*, 6725.
- [71] Zhensheng, J.; Chanjuan, X.; Qingmei, Z.; Feng, Y.; Jiazheng, Z.; Jinzhen, X. *J. Mol. Catal. A: Chem.* **2003**, *191*, 61.
- [72] Kempf, J. Y.; Silvi, B.; Dietrich, A.; Catlow, C. R. A.; Maigret, B. *Chem. Mater.* **1993**, *5*, 641.
- [73] Brázdová, V.; Ganduglia-Pirovano, M. V.; Sauer, J. *Phys. Rev. B* **2004**, *69*, 165420.
- [74] Gong, D.; Grimes, C. A.; Varghese, O. K.; Hu, W.; Singh, R. S.; Chen, Z.; Dickey, E. C. *J. Mater. Res.* **2001**, *16*, 3331.

- [75] Luo, Y.; Lee, S. K.; Hofmeister, H.; Steinhart, M.; Gösele, U. *Nano Lett.* **2004**, *4*, 143.
- [76] Zhensheng, J.; private communication.
- [77] Oh, D.-H.; Lee, Y. H. *Phys. Rev. B* **1998**, *58*, 7407.
- [78] Uddin, J.; Peralta, J. E.; Scuseria, G. E. *Phys. Rev. B* **2005**, *71*, 155112 and references therein.
- [79] Park, K.-T.; Novikov, D. L.; Gubanov, V. A.; Freeman, A. J. *Phys. Rev. B* **1994**, *49*, 4425.
- [80] Hass, K. C.; Carlsson, A. E. *Phys. Rev. B* **1992**, *46*, 4246.
- [81] Gonze, X.; Allan, D. C.; Teter, M. P. *Phys. Rev. Lett.* **1992**, *68*, 3603.
- [82] Waghmare, U. V.; Spaldin, N. A.; Kandpal, H. C.; Seshadri, R. *Phys. Rev. B.* **2003**, *67*, 125111.
- [83] Tagirov, V. K.; Chizhikov, D. M.; Kazenas, E. K.; Shubochkin, L. K.; *Zh. Neorg. Khim.* **1976**, *21*, 2565.
- [84] Latimer, W. M.; *Oxidation potentials*, 2nd Edition, Prentice-Hall, New York, 1952.
- [85] Lide, D. R. *Handbook of Chemistry and Physics*, 72nd Edition, Franklin, Bloomfield Hills, MI, 1991.
- [86] Brennan, D.; Hayward, D. O.; Trapnell, B. M. W. *Proc. R. Soc. Ser.* **1960**, *A256*, 81.
- [87] Saenger, K. L.; Cabral, C.; Lavoie, Jr. C.; Rossnagel, S. M. *J. Appl. Phys.* **1999**, *86*, 6084.
- [88] Zakharchenko, N. I. *Russ. J. of Appl. Chem.* **2001**, *74*, 1686.

- [89] Pies, W.; Weiss, A.; in *Landolt-Börnstein*, New Series; Hellwege, K.-H.; Hellwege, A. M., Eds; Springer-Verlag: Berlin, 1975; vol NS III/7b1, p 601.
- [90] Heilmann, P.; Heinz, K.; Müller, K. *Surf. Sci.* **1979**, *83*, 487.
- [91] Van Beurden, P.; Bunnik, B. S.; Kramer, G. J.; Borg, A. *Phys. Rev. Lett.* **2003**, *90*, 66106.
- [92] Hu, X.; Lin, Z. *Phys. Rev. B* **1995**, *52*, 11467.
- [93] Colen, R. E. R.; Christoph, J.; Peña, F.; Rotermund, H. H. *Surf. Sci.* **1998**, *408*, 310.
- [94] Dicke, J.; Rotermund, H. H.; Lauterbach, J. *Surf. Sci.* **2000**, *454-456*, 352.
- [95] McMillan, N.; Lele, T.; Snively, C.; Lauterbach, J. *Cat. Tod.* **2005**, *105*, 244.
- [96] Weaver, J. F.; Chen, J.-J.; Gerrard, A. L. *Surf. Sci.* **2005**, *592*, 83.
- [97] Deskins, N. A.; Lauterbach, J.; Thomson, K. *J. Chem. Phys.* **2005**, *122*, 184709.
- [98] Wulff, G. *Z. Kristallogr.* **1901**, *34*, 449.
- [99] Valkealahti, S.; Manninen, M. *Phys. Rev. B.* **1992**, *45*, 9459.
- [100] Reinhard, D.; Hall, B. D.; Berthoud, P.; Valkealahti, S.; Monot, R. *Phys. Rev. Lett.* **1997**, *79*, 1459.
- [101] Carlsson, P.-A.; Mollner, S.; Arnby, K.; Skoglundh, M. *Chem. Eng. Sci.* **2004**, *59*, 4313.
- [102] Wang, C.-B.; Yeh, C.-T. *Appl. Catal. A-General* **2001**, *209*, 1.
- [103] *CRC Handbook of Chemistry and Physics*; CRC Press: Boca Raton, 1995; p. 5-76.
- [104] Mendiara, T.; Alzueta, M. U.; Millera, A.; Bilbao, R. *Energy & Fuels*, **2004**, *18*, 619.

- [105] Harris, J.; Simon, J.; Luntz, A. C.; Mullins, C. B.; Rettner, C. T. *Phys. Rev. Lett.* **1991**, *67*, 652.
- [106] Crabtree, R. H. *Chem. Rev.* **1995**, *95*, 987.
- [107] Michaelides, A.; Liu, Z.-P.; Zhang, C. J.; Alavi, A.; King, D. A.; Hu, P. *J. Am. Chem. Soc.* **2003**, *125*, 3704.
- [108] Ullrich, F.; private communication.
- [109] Feibelman, P. J.; Hammer, B.; Nørskov, J. K.; Wagner, F.; Scheffler, M.; Stumpf, R.; Watwe, R.; Dumesic, J. *J. Phys. Chem. B* **2001**, *105*, 4018.
- [110] Olsen, R. A.; Philipsen, P. H. T.; Baerends, E. J. *J. Chem. Phys.* **2003**, *119*, 4522.
- [111] Sabatier, P. *La catalyse en chimie organique*, Berange, Paris, 1920.
- [112] Alavi, A.; Hu, P.; Deutsch, T.; Silvestrelli, P. L.; Hutter, J. *Phys. Rev. Lett.* **1998**, *80*, 3650.
- [113] Eichler, A.; Hafner, J. *Phys. Rev. B* **1999**, *59*, 5960.
- [114] Otto, J.; Thomas, W.; in *Landolt-Börnstein*, 6th edition; Hausen H., Ed; Springer-Verlag: Berlin, 1967; vol IV/4a, pp 295.
- [115] Gélin, P.; Primet, M. *Appl. Catal. B-Environ.* **2002**, *39*, 1.
- [116] Yazawa, Y.; Yoshida, H.; Hattori, T. *Appl. Catal. A-General* **2002**, *237*, 139.
- [117] Sabourault, N.; Mignani, G.; Wagner, A.; Mioskowski, C. *Org. Lett.* **2002**, *4*, 2117.

# Acknowledgements

I would like to thank Prof. Wolfgang Pompe for giving me the opportunity to work in this extremely exciting field, and all the colleagues at the Chair of Materials Science and Nanotechnology for the interesting exchanges of ideas and the nice working environment. Special thanks go also to Lucio Colombi Ciacchi, without whom this work would not have been possible, and to the High-Performance Computing Center of the TU Dresden for making huge computational resources available and for the outstanding technical support. I would also like to thank Francesco Seriani and Vineeth Surendranath for critically reading the manuscript.

The development of this work has been constantly influenced by discussions with and suggestions by colleagues at the Chair of Materials Science and Nanotechnology, as well as scientific partners at Namos GmbH, at Bosch GmbH, at the Institute of Genetics at the TU Dresden, at the Institute of Physical Chemistry at the TU Freiberg, at the Department of Physics at the TU Dresden and at the TASC Laboratory in Trieste.

I would like to thank the Theory of Condensed Matter group at the Cavendish Laboratory at the University of Cambridge for its hospitality in August 2003 and October 2004.